NASA/TM-2001-210830

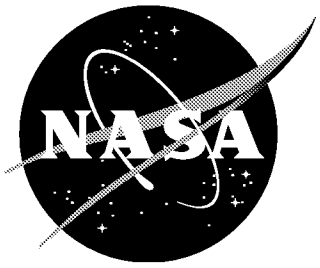

Fatigue Crack Growth Characteristics of Thin Sheet Titanium Alloy Ti 6-2-2-2-2

Stephen W. Smith and Robert S. Piascik
Langley Research Center, Hampton, Virginia

March 2001

The NASA STI Program Office ... in Profile

Since its founding, NASA has been dedicated to the advancement of aeronautics and space science. The NASA Scientific and Technical Information (STI) Program Office plays a key part in helping NASA maintain this important role.

The NASA STI Program Office is operated by Langley Research Center, the lead center for NASA's scientific and technical information. The NASA STI Program Office provides access to the NASA STI Database, the largest collection of aeronautical and space science STI in the world. The Program Office is also NASA's institutional mechanism for disseminating the results of its research and development activities. These results are published by NASA in the NASA STI Report Series, which includes the following report types:

- TECHNICAL PUBLICATION. Reports of completed research or a major significant phase of research that present the results of NASA programs and include extensive data or theoretical analysis. Includes compilations of significant scientific and technical data and information deemed to be of continuing reference value. NASA counterpart of peer-reviewed formal professional papers, but having less stringent limitations on manuscript length and extent of graphic presentations.

- TECHNICAL MEMORANDUM. Scientific and technical findings that are preliminary or of specialized interest, e.g., quick release reports, working papers, and bibliographies that contain minimal annotation. Does not contain extensive analysis.

- CONTRACTOR REPORT. Scientific and technical findings by NASA-sponsored contractors and grantees.

- CONFERENCE PUBLICATION. Collected papers from scientific and technical conferences, symposia, seminars, or other meetings sponsored or co-sponsored by NASA.

- SPECIAL PUBLICATION. Scientific, technical, or historical information from NASA programs, projects, and missions, often concerned with subjects having substantial public interest.

- TECHNICAL TRANSLATION. English-language translations of foreign scientific and technical material pertinent to NASA's mission.

Specialized services that complement the STI Program Office's diverse offerings include creating custom thesauri, building customized databases, organizing and publishing research results ... even providing videos.

For more information about the NASA STI Program Office, see the following:

- Access the NASA STI Program Home Page at ***http://www.sti.nasa.gov***

- E-mail your question via the Internet to help@sti.nasa.gov

- Fax your question to the NASA STI Help Desk at (301) 621-0134

- Phone the NASA STI Help Desk at (301) 621-0390

- Write to:
  NASA STI Help Desk
  NASA Center for AeroSpace Information
  7121 Standard Drive
  Hanover, MD 21076-1320

NASA/TM-2001-210830

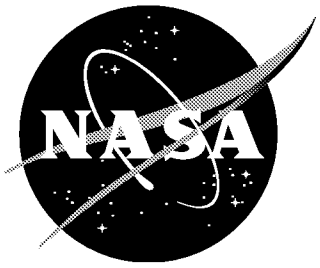

Fatigue Crack Growth Characteristics of Thin Sheet Titanium Alloy Ti 6-2-2-2-2

Stephen W. Smith and Robert S. Piascik
Langley Research Center, Hampton, Virginia

National Aeronautics and
Space Administration

Langley Research Center
Hampton, Virginia 23681-2199

March 2001

Available from:

NASA Center for AeroSpace Information (CASI)
7121 Standard Drive
Hanover, MD 21076-1320
(301) 621-0390

National Technical Information Service (NTIS)
5285 Port Royal Road
Springfield, VA 22161-2171
(703) 605-6000

Abstract

Fatigue crack growth rates of Ti 6-2-2-2-2 as a function of stress ratio, temperature (24 or 177 °C), tensile orientation and environment (laboratory air or ultrahigh vacuum) are presented. Fatigue crack growth rates of Ti 6-2-2-2-2 are also compared with two more widely used titanium alloys (Timetal 21S and Ti 6Al-4V). The fatigue crack growth rate (da/dN) of Ti 6-2-2-2-2 in laboratory air is dependent upon stress ratio (R), particularly in the near-threshold and lower-Paris regimes. For low R (less than approximately 0.5), da/dN is influenced by crack closure behavior. At higher R (> 0.5), a maximum stress-intensity factor (K_{max}) dependence is observed. Fatigue crack growth behavior is affected by test temperature between 24 and 177 °C. For moderate to high applied cyclic-stress-intensity factors (ΔK), the slope of the log da/dN versus log ΔK curve is lower in 177 °C laboratory air than 24 °C laboratory air. The difference in slope results in lower values of da/dN for exposure to 177 °C laboratory air compared to room temperature laboratory air. The onset of this temperature effect is dependent upon the applied R. This temperature effect has not been observed in ultrahigh vacuum. Specimen orientation has been shown to affect the slope of the log da/dN versus log ΔK curve in the Paris regime. The damaging effect of laboratory air is more pronounced for specimens with the applied load oriented 45° to the longitudinal and long transverse directions compared to fatigue crack growth in the T-L or L-T orientations.

Introduction

Titanium alloy systems are being considered for advanced supersonic aircraft components, because they have a higher specific strength and improved thermal stability compared to conventional aluminum alloys. Some components on supersonic airframes, for example skin on leading edges, may operate at temperatures greater than 130 °C for tens-of-thousands of hours; which precludes the use of conventional aluminum alloys. The objective of this work is to characterize the fatigue crack growth behavior of one such advanced titanium alloy sheet, Ti - 6 Al - 2 Zr - 2 Cr - 2 Sn - 2 Mo (Ti 6-2-2-2-2) and to compare this behavior with two more widely studied sheet materials, a β titanium alloy (Timetal 21S) and another α+β alloy (Ti 6Al-4V). Characterization of the fatigue crack growth behavior in an active environment (air) compared to an inert environment (ultrahigh vacuum) will be used to develop an understanding of the environmental interactions which influence long term durability [1-4].

Materials Processing and Characterization

The Ti 6-2-2-2-2 alloy product studied was a 1.65 mm (0.065 inch) thick cross rolled sheet. The sheet was hot rolled at 927 °C (1700 °F) and solution annealed at 899 °C (1650 °F) for 30 minutes, followed by an aging treatment at 510 °C (950 °F) for 10 hours (in all cases the sheet material was processed in packs of several sheets which were air cooled following all heat treatments). The chemical composition and β transus are shown in Table I. The as-received sheet contained primary α grains of less than 10 μm, with transformed β colonies, as shown in Figure 1 (the primary α grains appear lighter than the transformed colonies). Grains were pancake shaped, elongated in the longitudinal (L) and long transverse (T) directions. While this microstructure was fairly uniform, there was evidence of some highly elongated primary α grains, Figure 2. The Ti 6-2-2-2-2 alloy contains a higher fraction of β phase than does the near α (lean in retained β) Ti 6Al-4V alloy, which has a small amount of acicular α and some intergranular β. Chemical compositions of these alloys are given in Table I. Grain sizes, phase composition, and morphology of the three alloys are listed in Table II.

Table III summarizes room temperature L and T mechanical properties for Ti 6-2-2-2-2, Timetal 21S, and Ti 6Al-4V. The Timetal 21S, β-Ti alloy, exhibits the greatest ultimate (σ_{UTS}) and yield (σ_{ys}) strengths followed by the α+β alloy, Ti 6-2-2-2-2, and the near α Ti 6Al-4V alloy. The additional β present in the Ti 6-2-2-2-2, results in a significant increase in strength, compared to the near α alloy Ti 6Al-4V. The elastic modulus (E) for the three sheet products does not follow the same trend, as does the strength in the longitudinal and transverse axes. Ti 6-2-2-2-2 was found to have the highest modulus followed by the Ti 6Al-4V and the Timetal 21S sheets.

Rolled α+β alloys develop a textured microstructure with preferential alignment of the basal planes (0002) in the hexagonal α phase [5, 6]. A texture analysis was performed on the Ti 6-2-2-2-2 sheet and is presented in Figure 3. The maximum intensities for the (0002) normal were found to be rotated approximately 35° from the short transverse (S) direction towards the T and approximately 30° from the S to the L direction. The texture was examined at the middle of the sheet thickness (t/2) as well as the t/4 plane, with both locations exhibiting a similar texture. It is common for the (0002) poles of rolled alloys containing a hexagonal phase to be concentrated 30 to 40° from the sheet normal in the T direction [6]. This preferential alignment

of (0002) has been attributed to the competition between $\{0002\}\ <11\bar{2}0>$ slip, rotating the basal poles toward the sheet normal and $\{11\bar{2}2\}$ twinning, rotating the basal poles towards the transverse direction [6]. Since the Ti 6-2-2-2-2 sheet was cross rolled, the basal planes were rotated 30° to 40° towards both the L and T axes from the S axis. The observed texture produced basal planes of the α phase oriented nearly equally with respect to the L and T directions. Consequently, a crack growing normal to the tensile axis in a T-L oriented (T tensile axis with the crack growing in the L direction) fatigue crack growth specimen would encounter roughly the same microstructure as a crack growing normal to the tensile axis in a L-T oriented (L tensile axis with the crack growing in the T direction) specimen. Therefore, comparison of the fatigue crack growth behavior for only T-L and L-T oriented mechanical test specimens is not adequate to evaluate the effect of texture on the fatigue crack growth behavior for the cross rolled Ti 6-2-2-2-2 sheet product. Accordingly, fatigue crack growth rate tests for specimens with the applied load oriented 45° to the longitudinal and long transverse directions will also be presented.

Experimental

All fatigue crack growth testing was performed using computer-controlled, closed-loop, servo-hydraulic machines, operating under load control, and using a sinusoidal waveform. Laboratory air and ultrahigh vacuum testing was conducted at room (24 °C) and elevated temperature (177 °C). Inert environment testing was conducted in an ultrahigh vacuum, metal-to-metal sealed, stainless steel chamber with a baseline pressure less then 7×10^{-7} Pa ($< 5 \times 10^{-9}$ Torr). A platinum electrode furnace contained in the vacuum chamber was used for elevated temperature testing for the inert environment.

Fatigue crack growth tests were conducted using eccentrically-loaded single edge notch tensile (ESE(T)) specimens (formally known as extended compact tension, EC(T)), shown in Figure 4. The final thickness (B) of the specimens tested in this study was 1.52 mm. Crack-tip stress-intensity factor (K) controlled testing was performed by continuously determining crack length (a) using a compliance based measurement technique. Displacement measurements were made using either a clip gage placed across the crack mouth using integrally machined knife edges, shown in detail A of Figure 4, or a strain gage bonded to the back-face surface of the specimen, shown in Figure 4. All near-threshold tests were conducted with a strain gage bonded

to the back-face surface of the specimen to eliminate anomalous crack-tip loading which can be introduced when using a clip gage. Automated crack length determinations make it possible to vary the amplitude of a sinusoidal load spectra in order to obtain the desired cyclic-stress-intensity factor (ΔK) during fatigue testing. Compliance and stress-intensity factor solutions for the ESE(T) specimen are presented in Appendix A.

To verify automated compliance based crack length determinations, visual surface crack length measurements were performed periodically during the tests using a 20X telescope mounted on a traveling stage with a resolution of $\pm$ 25 μm ($\pm$ 0.001 inch) for tests conducted in lab air, and using a long focal length microscope ($\approx$ 400X) for tests conducted in the vacuum chamber. Following each test, the visual crack length measurements and a final fracture surface crack length measurement were used to make small (typically 0.5 % error) corrections to the compliance based crack length determinations by linear interpolation.

Fatigue crack growth rate data was generated by performing both K-increasing and K-decreasing tests at a constant stress ratio (R), in accordance with ASTM standard E 647 [7]. K-decreasing tests were conducted to the fatigue crack growth threshold (defined as a fatigue crack growth rate, da/dN, approximately 10^{-10} m/cycle) at a normalized K-gradient (C) of -0.079 mm^{-1} (-2 in^{-1}). All K-increasing tests were conducted at a C of 0.16 mm^{-1} (4 in^{-1}). Two K-increasing tests were performed in laboratory air to insure reproducibility. Additionally, a portion of the data generated during the K-decreasing test was duplicated during a K-increasing test to insure reproducibility for these two test profiles. The test parameters (i.e., frequency and C) were consistent from specimen to specimen in order to quantify the effect of material chemistry, stress ratio, temperature, specimen orientation and test environment on fatigue crack growth rate.

Decreasing-ΔK tests were also performed using a constant-K_{max} (increasing-R) method [8, 9]. These increasing-R tests result in high R (typically R > 0.9) as threshold is approached. During constant-K_{max} testing, the minimum applied stress-intensity factor (K_{min}) increases with decreasing ΔK, making it possible to maintain a K_{min} which is greater than the crack-opening stress-intensity factor (K_{op}), resulting in closure-free near-threshold fatigue crack growth rates [8, 9].

To make direct comparisons of fatigue crack growth rates for specimens tested under various conditions (stress ratio, temperature, orientation and environment), the extrinsic effect of crack closure has to be considered. Closure is produced by the premature contact of fatigue-

crack surfaces, resulting in an effective ΔK ($\Delta K_{eff} = K_{max} - K_{op}$) that is less than the applied ΔK [10]. Load-displacement data from either the back-face or front-face displacement gage was analyzed using the offset technique described in ASTM standard E 647 [7] to determine opening loads. To insure the accuracy of the automated opening load determinations, additional load-displacement data were acquired and an opening load was determined using Elber's reduced-displacement technique [11]. An opening load determined using the reduced-displacement technique was compared to five opening load predictions determined by the automated system for five selected offset percentages (1, 2, 4, 8, and 16%) at the same applied ΔK value. The offset percentage, which resulted in the best correlation of K_{op} with the reduced-displacement result, was used to calculate the appropriate ΔK_{eff}.

Results and Discussion

To develop a comprehensive understanding of the fatigue crack growth characteristics for a thin sheet Ti 6-2-2-2-2 alloy, several factors that can affect fatigue crack growth rate have been examined. In addition, the fatigue crack growth behavior of Ti 6-2-2-2-2 at room temperature has been compared to two more commonly used titanium alloys. The results are detailed in five sections below; 1) Comparison of Room Temperature da/dN, 2) Effect of Stress Ratio, 3) Effect of Temperature, 4) Effect of Crack Path Orientation, and 5) Effect of Environment. A sixth section, which includes fractography, has been supplied to aid in identifying the causal effects for the test conditions examined.

Comparison of Room Temperature da/dN

Figure 5a shows results for T-L oriented Ti 6-2-2-2-2, Timetal 21S, and Ti 6Al-4V fatigue crack growth rate tests conducted in room temperature laboratory air at a frequency of 5 Hz and R = 0.5. No detectable crack closure was observed, using compliance methods, for all three materials during R = 0.5 tests. Therefore, the differences in fatigue crack growth characteristics observed in Figure 5a are believed to be a result of intrinsic properties and not extrinsic crack wake effects (closure). For ΔK less than approximately 4 or 5 MPa$\sqrt{m}$, the intrinsic fatigue crack growth rate of Ti 6-2-2-2-2 was lower than Timetal 21S. For $\Delta K > 4$ or 5 MPa$\sqrt{m}$, the fatigue crack growth characteristics of Ti 6-2-2-2-2 and Timetal 21S were nearly

identical. Both higher strength alloys (Ti 6-2-2-2-2 and Timetal 21S) exhibited increased fatigue crack growth rates compared to Ti 6Al-4V. In the region of rapid crack growth rates ($\Delta K > 20$ MPa$\sqrt{m}$), the alloys having lower fracture toughness (Ti 6-2-2-2-2 and Timetal 21S) compared to Ti 6Al-4V exhibited accelerated intrinsic da/dN.

The fatigue crack growth behavior of Ti 6Al-4V and Timetal 21S determined in this study are compared with results from the literature in Figures 5b and 5c, respectively. Figure 5b is a plot comparing room temperature laboratory air fatigue crack growth rate data for the present 1.52 mm thick Ti 6Al-4V sheet with 9.65 mm thick Ti 6Al-4V plate at R = 0.5 [12]. For $\Delta K <$ 13 MPa$\sqrt{m}$, similar fatigue crack growth characteristics are observed for Ti 6Al-4V sheet and plate. For $\Delta K > 13$ MPa$\sqrt{m}$, the fatigue crack growth rate for the sheet product is lower than the fatigue crack growth rate for the plate material. These results are consistent with previously reported observations [13]. Figure 5c shows fatigue crack growth characteristics for Timetal 21S for $\Delta K > 7$ MPa$\sqrt{m}$ in room temperature laboratory air. Here, da/dN data at f = 5 Hz are in excellent agreement with data from the literature at f = 30 Hz [14]. Results shown in Figure 5c reveal no effect of loading frequency (5 and 30 Hz) for $\Delta K > 7$ MPa$\sqrt{m}$.

Effect of Stress Ratio

Figure 6 shows room temperature laboratory air fatigue crack growth rate data for Ti 6-2-2-2-2 ranging from 10^{-11} to 10^{-5} m/cycle for tests conducted at R = 0.1 (circle symbols) and R = 0.5 (square symbols). Also plotted in Figure 6 are the R = 0.1 data corrected for crack closure (diamond symbols). The data represented by each symbol in Figure 6 are results for three tests. A downward arrow is used to indicate the start of a K-decreasing test for each stress ratio and upward arrows are used to indicate the start of two K-increasing tests for each stress ratio. Fourteen load-displacement measurements, noted as 1 through 14 in Figure 6, were acquired during the R = 0.1 tests. For each load-displacement measurement, an opening load was determined using Elber's reduced-displacement method [11]. Some representative load versus strain deviation curves are supplied in Appendix B. Figures B1 and B2 are two reduced-strain curves generated for the R = 0.1 tests labeled in Figure 6. Opening loads determined from the reduced-displacement method are compared with opening load values for five different offset levels [7] calculated by the computer-controlled testing system. The opening loads determined

from the fourteen load-displacement measurements at R = 0.1 compared most favorably with the opening load determinations at an offset of 1 %. Therefore, the closure corrected R = 0.1 (ΔK_{eff}) results shown in Figure 6 were calculated using the opening loads at a 1 % offset. The offset and reduced-displacement techniques were also used to determine opening loads for the R = 0.5 fatigue crack growth tests. Acquisition of ten load-displacement measurements are noted as A through J in Figure 6. No evidence of crack closure was observed during fatigue crack growth testing at R = 0.5, as revealed by the vertical load versus strain deviation plot shown in Figure B3. The excellent correlation between the constant R = 0.5 test data and the ΔK_{eff} (R = 0.1) based determinations, shown in Figure 6, and the fact that no crack closure was detected during constant R = 0.5 tests suggests that the constant R = 0.5 data represents the closure-free (intrinsic) fatigue crack growth characteristics of Ti 6-2-2-2-2 in room temperature laboratory air. However, it will be shown later, that the compliance techniques have not accounted for all of the closure present for these tests.

The fatigue crack growth characteristics of T-L oriented Ti 6-2-2-2-2 for the lower-Paris to threshold regime ($\Delta K \leq 10$ MPa$\sqrt{m}$) are shown in Figure 7 for a wide range of stress ratios. Decreasing-ΔK tests were conducted at constant K_{max}, R ranging from approximately 0.15 to 0.95, as well as constant stress ratios, R = 0.1 and 0.5. Three data points on the constant-K_{max} curves in Figure 7 for ΔK between 5.5 and 9.5 MPa$\sqrt{m}$ have been encircled. At these three data points, additional data with similar stress ratios are present for constant-R tests. Here, excellent agreement in da/dN is observed for the different test methods. For example, similar fatigue crack growth rates are observed for the constant-K_{max} (11 MPa$\sqrt{m}$) testing at R = 0.5 and 0.15 compared to fatigue crack growth rates obtained for constant-R testing at R = 0.5 and 0.1, respectively. At very low values of ΔK, the three constant-K_{max} tests shown in Figure 7 produce accelerated da/dN compared to the two constant-R tests. A line of constant da/dN at 1×10^{-10} m/cycle has been indicated on Figure 7. According to ASTM E 647 [7] this fatigue crack growth rate can be used to estimate fatigue crack growth threshold (ΔK_{th}). The three values of ΔK identified along the x-axis in Figure 7 represent the intercepts of the fatigue crack growth test results (K_{max}= 16.5 MPa$\sqrt{m}$, R = 0.5, and R = 0.1) with da/dN = 1×10^{-10} m/cycle. Estimated intercepts of the five curves shown in Figure 7 as well as for constant-K_{max} tests of 3.85 and 6.6 MPa$\sqrt{m}$ with 1×10^{-10} m/cycle are presented as ΔK_{th} in Table IV. This data indicates a

decreasing ΔK_{th} with increasing K_{max}. As shown in Figure 6, the difference in ΔK_{th} for R = 0.1 and 0.5 appears to be a result of crack closure. However, the further decrease in ΔK_{th} observed for the three closure-free K_{max} tests presented in Figure 7 are consistent with recent research [15, 16] indicating an effect of applied K_{max} and not consistent with the view of a single intrinsic fatigue crack growth rate curve [10].

One potential effect that could influence the results of the constant-K_{max} tests presented in Figure 7 is an apparent decrease in toughness with crack length. To examine this effect in Ti 6-2-2-2-2, several specimens were fatigue cracked to different lengths and then pulled to failure at a constant crosshead rate. Results of apparent fracture toughness (K_c) versus a/W are presented for four T-L oriented Ti 6-2-2-2-2 specimens in Figure 8. Here an obvious trend of decreasing stress-intensity factor at failure is observed with increasing crack length. To minimize any potential effect of this observation, the fatigue results presented within this paper are only shown for values of a/W less than 0.75 and the applied K_{max} was always less than half the apparent fracture toughness. Additionally, the results for constant-K_{max} tests presented in Figure 7 and for subsequent results were acquired using multiple specimens, and the trend observed (decreasing ΔK_{th} with increasing K_{max}) could not be related to the crack length or apparent fracture toughness for each test.

Values of ΔK_{th} plotted against applied K_{max} in Figure 9 (represented as circle symbols) reveal two distinct regions [17, 18]. For low values of K_{max} (< 4.6 MPa$\sqrt{m}$), a relatively large increase in ΔK_{th} is observed with decreasing K_{max} (dashed linear regression line). For values of K_{max} greater than approximately 4.6 MPa$\sqrt{m}$, a more subtle yet distinct decrease in ΔK_{th} is observed for increasing K_{max} (dotted linear regression line). Here, the large increase in ΔK_{th} with decreasing K_{max} (for K_{max} < 4.6 MPa$\sqrt{m}$) is dominated by crack closure, while the subtle decrease in ΔK_{th} (K_{max} > 4.6 MPa$\sqrt{m}$) is a true K_{max} effect [17, 18]. The results shown in Figure 9 suggest that closure was present at threshold for R = 0.5 (ΔK = 2.09 MPa$\sqrt{m}$, K_{max} = 4.18 MPa$\sqrt{m}$), even though no closure was measured using the far-field displacement techniques described above. This discrepancy is believed to be due to a lack of crack-tip displacement measurement resolution using far-field displacement gages such as a back-faced strain gage or front-face clip gage. By extending the regression line for the K_{max}-affected region to values of

K_{max} < 4.6 MPa$\sqrt{m}$, closure-free values of ΔK_{th} ($\Delta K_{th,\ eff}$) can be predicted (represented as triangle symbols in Figure 9).

Curves of ΔK versus K_{max} were generated for a total of twenty values of da/dN from 1 x 10^{-10} to 1 x 10^{-7} m/cycle for Ti 6-2-2-2-2. Figure 10 contains data for four of these values of da/dN. At each value of da/dN data are fit using two linear regression lines. At low values of K_{max}, a relatively large increase in ΔK is observed with decreasing K_{max} (dashed linear regression lines). For larger values of K_{max}, a distinct change in slope is observed (dotted linear regression lines). To delineate between the two regions of crack growth, solid line segments are drawn connecting the intercepts between the closure-dominated (Region A, dashed lines) and closure-free (Region B, dotted lines) data. Plots of ΔK versus K_{max} can thus be used as an empirical method to determine whether fatigue crack growth rate data are influenced by crack closure without relying on displacement measurements from a far-field displacement gage.

Figure 11 is a plot of da/dN versus ΔK for tests at three different conditions (constant K_{max} = 22 MPa$\sqrt{m}$, R = 0.1, and R = 0.5). Also shown are two ΔK_{eff} curves for the two constant-R tests that were generated using K_{op} determined by the empirical threshold method described above for each of the twenty values of da/dN selected. These curves are considered as a boundary for closure affected data. All of the data points to the right of the two closure-free curves are affected by closure and the data to the left of the curves are not affected by closure. Values of da/dN, applied ΔK and closure-free ΔK for da/dN less than 1 x 10^{-7} m/cycle for R = 0.5 and 0.1 are presented in Appendices C and D, respectively. It should be noted that the empirical threshold method results are contrary to standard ASTM crack closure determinations shown above. Figure 11 shows that near-threshold (ΔK < 3.5 MPa$\sqrt{m}$) fatigue crack growth rates at R = 0.5 are influenced by crack closure.

Effect of Temperature

Figures 12 and 13 compare room temperature (24 °C) and elevated temperature (177 °C) fatigue crack growth rate data at R = 0.1 and R = 0.5, respectively. For R = 0.1 (Fig. 12), the fatigue crack growth rates at 24 °C and 177 °C are similar for ΔK < 25 MPa$\sqrt{m}$. For ΔK > 25 MPa$\sqrt{m}$, room temperature fatigue crack growth rates are accelerated compared to that observed at 177 °C. The R = 0.5 fatigue crack growth rate characteristics shown in Figure 13 reveals

room temperature da/dN is accelerated compared to crack growth at 177 °C for $\Delta K > 7$ MPa$\sqrt{m}$. A comparison of the results shown in Figures 12 and 13 suggests a stronger influence of temperature on fatigue crack growth rates at R = 0.5. Over the entire range of ΔK examined, no closure was observed for testing at R = 0.5 using far-field compliance based closure techniques; however, closure was measured for R = 0.1. To further evaluate the fatigue crack growth behavior in the lower-Paris to threshold regime at 177 °C, several constant-K_{max} decreasing-ΔK tests were performed (Fig. 14). Threshold ΔK values at 177 °C for each test are shown in Table V. The 24 °C and 177 °C threshold data plotted as ΔK_{th} versus K_{max} in Figure 15, exhibit similar trends for the closure-dominated (dashed linear regression lines) and closure-free (dotted linear regression lines) regions. Figure 16 is a plot of ΔK versus K_{max} data at a fatigue crack growth rate of 1×10^{-8} m/cycle. Temperature (24 to 177 °C) is shown to have little influence on the closure-dominated (dashed linear regression lines) region. However, for the closure-free data (dotted linear regression lines), a temperature dependence is indicated as a difference in slope for the data at the two temperatures examined. Applied K_{max} has less of an influence on fatigue crack growth behavior at 177 °C than at room temperature (Fig. 16). As was done at room temperature, plots of ΔK versus K_{max} were produced at twenty values of da/dN between 1×10^{-10} and 1×10^{-7} m/cycle. From these plots closure-free fatigue crack growth rate data for R = 0.1 and 0.5 were generated. Values of da/dN, applied ΔK and closure-free ΔK for da/dN less than 1×10^{-7} m/cycle for R = 0.5 and 0.1 tests at 177 °C are supplied in Appendices E and F, respectively.

Figures 12 and 13 indicate an increase in temperature from 24°C to 177°C can result in a decrease in da/dN for Ti 6-2-2-2-2 in laboratory air. While increasing temperature has been shown to produce an increase in da/dN for several materials [19, 20], previous studies of $\alpha+\beta$ titanium alloys have also observed a decrease in da/dN with increasing temperature for certain conditions [21, 22]. Decreasing da/dN with increasing temperature has only been observed over a selected temperature range (approximately 0 to 150°C)[21]. Several reasons for this effect have been proposed [21, 22]; however, there has been no definitive evidence to support any one theory. This will be discussed in further detail in a later section (Effect of Environment).

Effect of Crack Path Orientation

Fatigue crack growth rates of T-L, L-T and 45° oriented Ti 6-2-2-2-2 specimens at room temperature and T-L and 45° oriented Ti 6-2-2-2-2 specimens at 177 °C are shown in Figures 17 and 18, respectively. At 24 °C, T-L and L-T orientations exhibit similar fatigue crack growth rate characteristics except at moderate values of ΔK (between 7.7 and 16.5 MPa$\sqrt{m}$) where the T-L orientation was found to have a slightly higher (approximately 1.5 times greater) da/dN compared to the L-T orientation. The fatigue crack growth behavior observed for the 45° orientation is different than the behavior for either the T-L or L-T orientations (Fig. 17). The T-L and L-T Paris regime fatigue crack growth curves are approximately described by a $\Delta K^{2.6}$ power law while the 45° orientation is characterized by a single $\Delta K^{4.5}$ power law. The fatigue crack growth characteristics at elevated temperature (Fig. 18) are described by a $\Delta K^{2.2}$ power law for the T-L orientation and a $\Delta K^{3.5}$ power law for the 45° orientation.

Figure 19 is a plot of lower-Paris to threshold regime da/dN versus ΔK data for L-T oriented specimens. As was observed for the T-L orientation, ΔK_{th} is shown to decrease with increasing K_{max}. Table VI lists values of ΔK_{th} for each of the tests represented in Figure 19. The ΔK_{th} values are approximated using the ASTM guideline of 1×10^{-10} m/cycle [7]. Figure 20 is a plot of ΔK_{th} versus K_{max} for the L-T data listed in Table VI and T-L data listed in Table IV. Similar trends are observed for the two orientations, indicating nearly identical behavior for both the closure-dominated (dashed linear regression lines) and closure-free (dotted linear regression lines) regions. These observations have been made for values of da/dN up to 7×10^{-9} m/cycle. The similarity between the T-L and L-T oriented specimens can be attributed to the cross-rolling procedure used to fabricate the Ti 6-2-2-2-2 sheet. The basal planes in the α phase are preferentially rotated 30 to 40° towards both the longitudinal and long transverse axes from the short transverse axis (Fig. 3). Consequently, fatigue cracks growing in T-L and L-T specimens will intersect nearly identical crystallographic morphologies resulting in similar fatigue crack growth behavior.

The difference in the ΔK power law for 45° oriented specimens compared to either T-L or L-T oriented specimens (Figs. 17 and 18) is similar to results previously presented for highly textured Ti 6Al-4V [23, 24]. In this previous study, the fatigue crack growth behavior of specimens machined from a rolled bar product with six different orientations were examined. A

$\Delta K^{2.5}$ power law approximated the Paris regime fatigue crack growth data for three of the orientations, while a $\Delta K^{(3.1 \text{ to } 4.1)}$ power law characterized the other three orientations. The lower exponent was observed when the α grains were oriented such that the maximum applied shear stress was very close to the primary slip plane in the slip direction [23, 24]. However, when the crystallographic slip systems were not aligned with the crack tip shear stresses, a larger exponent for the power law was obtained [23, 24].

Effect of Environment

Figure 21 compares room and elevated temperature fatigue crack growth characteristics of Ti 6-2-2-2-2 in laboratory air and ultrahigh vacuum ($< 7 \times 10^{-7}$ Pa) for R = 0.5. Fatigue crack growth rates in laboratory air are three to five times greater at room temperature and two to four times greater at 177 °C compared to ultrahigh vacuum for 5 MPa$\sqrt{m}$ < ΔK < 17 MPa$\sqrt{m}$. Environmental effects are minimized at rapid crack growth rates (ΔK > 17 MPa$\sqrt{m}$); where room temperature and elevated temperature da/dN in laboratory air converge with their respective vacuum fatigue crack growth rates. For 7 MPa$\sqrt{m}$ < ΔK < 17 MPa$\sqrt{m}$, a temperature effect is observed in laboratory air while there is little difference in fatigue crack growth rate data obtained at 24 and 177 °C in ultrahigh vacuum. This suggests that the temperature effect observed in laboratory air, for ΔK < 17 MPa$\sqrt{m}$, is related to the environmentally assisted processes developed in laboratory air. However, the temperature effect for ΔK > 17 MPa$\sqrt{m}$ is a result of an apparent increase in toughness as temperature is increased [13].

As stated earlier, a similar temperature effect, i.e. decreasing da/dN with increasing temperature, has been observed for α+β titanium alloys in this temperature range [21, 22]. While several potential causes were discussed, these papers proposed that stress induced hydride formation along α / β interfaces within the cyclic plastic zone is the most likely cause. It has been argued in these references that as temperature is increased above room temperature to approximately 150°C, the solubility of hydrogen within the titanium matrix will be increased sufficiently to reduce the potential for hydride formation. This argument can be used to help support the existence of a temperature effect in laboratory air while having no temperature effect in ultrahigh vacuum. However, if this mechanism were operative, one would expect to see evidence of intergranular fatigue fracture in laboratory air at room temperature and a more

ductile appearance at 177°C. Fractography presented in the section entitled Fractographic Observations does not support this argument.

Fatigue surfaces were produced in a high purity water vapor environment of 67 Pa at 24 and 177°C. The fatigue surfaces were then studied using X-ray Photoelectron Spectroscopy (XPS). Figures 22a and b shows the O^{1s} photoelectron spectra (represented by open circles) for the surfaces produced at 24 and 177°C, respectively. Each O^{1s} spectra was curve fit using constituent gaussian peaks (dashed lines) and the sum of the constituent peaks are also presented (solid lines). At 24°C (Fig. 22a) and 177°C (Fig. 22b), three constituent peaks are identified. The centers for each of the three constituent peaks are in good agreement with published binding energies for oxygen in adsorbed water (533.5 eV), an hydroxide (532.0 eV) and an oxide (530.5 eV) (identified with dotted lines) [25, 26]. The height of the constituent peaks identified as binding energies of oxygen in water and an hydroxide are found to have nearly the same ratio to one another at 24 and 177°C. However, the relative height of the peak associated with the oxygen binding energy in an oxide is greater at 177°C than at room temperature. This indicates that an hydroxide film dominates the surface when exposed to a water vapor environment at 24°C, while an oxide can readily form at 177°C. Therefore, it would appear that the temperature effect observed for fatigue crack growth rate in laboratory air is a direct result of the surface film formed at the growing fatigue crack. It is unclear if the different surface films directly affect the mechanical behavior of the crack tip or the increased oxide formed on the crack surfaces limit the amount of hydrogen absorbed in the cyclic plastic zone.

Figure 23 compares the fatigue crack growth characteristics of 45° oriented specimens in laboratory air and ultrahigh vacuum at room temperature. The ultrahigh vacuum data in Figure 23 represents two fatigue crack growth rate tests. During the K-increasing test the fatigue crack propagated at an angle of approximately 15° to the loading axis normal. To determine the reproducibility of the test, a K-decreasing ($C = -0.079\ mm^{-1}$) test was conducted on the same specimen. The propagating fatigue crack remained within 8° of the loading axis normal for the K-decreasing test. While a small difference in fatigue crack growth rates is shown for $7\ MPa\sqrt{m} < \Delta K < 10\ MPa\sqrt{m}$ (Fig. 23), the general fatigue crack growth behavior for the two tests are very consistent. A comparison of the vacuum and laboratory air fatigue crack growth characteristics shows minimal environmental effect for $\Delta K > 10\ MPa\sqrt{m}$. However, for $\Delta K < 10\ MPa\sqrt{m}$, a

strong environmental effect is observed. For $\Delta K = 7$ MPa$\sqrt{m}$, the fatigue crack growth rate for the 45° orientation is accelerated by a factor of twenty in air compared to vacuum. A similar comparison for the T-L orientation at 24 °C (Fig. 21), reveals an increase by a factor of three in air rates compared to vacuum (da/dN at $\Delta K = 7$ MPa$\sqrt{m}$).

Fractographic Observations

Fatigue crack surfaces were examined using a scanning electron microscope (SEM). Figures 24a and b are micrographs showing fatigue crack surfaces produced in laboratory air for $\Delta K = 19.8$ MPa$\sqrt{m}$, R = 0.5 and 5 Hz at room and elevated temperature, respectively. Fatigue surfaces produced at room temperature (Fig. 24a) exhibit a ductile appearance. At 177 °C (Fig. 24b), much of the fatigue surface was similar to that produced at room temperature. However, there were also smooth regions (marked with arrows on Figure 24b) running parallel to the crack growth direction. These smooth transgranular facets are present between the t/4 and 3t/4 planes through the specimen thickness. These flat regions are most prevalent in the regions where groups of elongated α grains were observed (Fig. 2). Differences in the fatigue surfaces are more apparent when viewed at higher magnification (Figs. 25a and b). Here, ductile tearing features are clearly present at room temperature (Fig. 25a), with mating features present on the conjugate surface. Examination of the transgranular facets at elevated temperature reveals the presence of parallel slip traces oriented approximately 30° from the crack growth direction (Fig. 25b). These observations for the smooth regions are consistent with quasi-cleavage of the elongated primary α [27]. Due to the highly textured nature of this material and the grouping of elongated primary α grains, these smooth regions can consist of cleavage facets for several grains.

Fatigue surfaces produced in ultrahigh vacuum were also examined to distinguish the effects of temperature and environment. Figures 26a and b are micrographs for specimens tested in ultrahigh vacuum at R = 0.5 and 5 Hz at room and elevated temperature, respectively. Each of the micrographs were taken in a region where ΔK was approximately 16.8 MPa$\sqrt{m}$. Fatigue surfaces produced at room temperature (Fig. 26a) were ductile in appearance, with ductile features appearing similar to the fatigue surface produced at room temperature in laboratory air (Fig. 24a). At 177 °C (Fig. 26b), small-elongated features were observed. However, these

features were not as large or abundant as those produced at 177 °C in laboratory air (Fig. 24b). Examination of these surfaces at higher magnification reveals a uniform and ductile surface is produced at room temperature and at 177°C in ultrahigh vacuum. These surfaces are comparable to those produced in laboratory air at 24°C (Fig. 25a).

The fatigue surfaces produced at 24 °C and 177 °C in ultrahigh vacuum at 16.8 MPa$\sqrt{m}$ (Fig. 26) are very similar in appearance to one another; while those produced in laboratory air at 24 °C and 177 °C for ΔK = 19.8 MPa$\sqrt{m}$ (Figs. 24 and 25) reveal distinct differences. These observations compare favorably with the fatigue crack growth rate data presented in Figure 21. In the inert environment, fatigue crack growth rates at 24 °C and 177 °C are roughly the same for applied ΔK values up to approximately 17 MPa$\sqrt{m}$ at R = 0.5. However, in laboratory air, fatigue crack growth rates at 177 °C become increasingly lower with increasing ΔK compared to fatigue crack growth rates at 24 °C for all applied ΔK greater than 7 MPa$\sqrt{m}$ at R = 0.5. Therefore, morphology of the fatigue surfaces helps to support the observations previously stated for Figure 21. Namely, temperature between 24 °C and 177 °C has very little affect on the intrinsic fatigue crack growth behavior of Ti 6-2-2-2-2 for ΔK < 19.8 MPa$\sqrt{m}$ at R = 0.5. However, in laboratory air, fatigue crack growth rates decrease with increasing temperature in the K_{max}- affected region.

Summary

1. For ΔK greater than 4.4 MPa$\sqrt{m}$, Ti 6-2-2-2-2 has a comparable fatigue crack growth rate to Timetal 21S sheet. Ti 6Al-4V sheet has a lower fatigue crack growth rate than either Ti 6-2-2-2-2 or Timetal 21S in room temperature laboratory air. In the near-threshold regime (ΔK less than 5 MPa$\sqrt{m}$) the fatigue crack growth rate was found to decrease with an increasing fraction of α phase (i.e. $da/dN_{Timetal\ 21S} > da/dN_{Ti\ 6\text{-}2\text{-}2\text{-}2\text{-}2} > da/dN_{Ti\ 6Al\text{-}4V}$).

2. Fatigue crack growth rate data for several values of R or K_{max} plotted as ΔK versus K_{max}, can be used to identify closure affected and closure-free fatigue crack growth rate data for Ti 6-2-2-2-2.

3. A stress ratio effect has been observed for Ti 6-2-2-2-2 for all loading conditions. While this effect is smaller for closure-free data than for closure-dominated data, a non-zero slope is

observed for all data presented as ΔK versus K_{max} for a selected da/dN. The empirical technique described in this paper makes it possible to delineate closure-free and closure-dominated K_{max} effects. This delineation is not possible using the ASTM suggested crack closure measurement technique.

4. For ΔK greater than 7 MPa$\sqrt{m}$ (R = 0.5), the fatigue crack growth rate for Ti 6-2-2-2-2 in 177 °C laboratory air is less than room temperature laboratory air. An apparent increase in toughness with temperature is observed for $\Delta K > 17$ MPa$\sqrt{m}$ (R = 0.5) in ultrahigh vacuum. However, a temperature dependence is not observed for $\Delta K < 17$ MPa$\sqrt{m}$. Therefore, the temperature dependence observed in laboratory air is a result of environmental interactions during fatigue cycling.

5. The fatigue crack growth characteristics of cross-rolled Ti 6-2-2-2-2 sheet are dependent upon specimen orientation. While the fatigue crack growth behavior of T-L and L-T oriented specimens are very similar, the fatigue behavior of 45° oriented specimens are very different. In the Paris regime, the slope of the log da/dN versus log ΔK curve is much higher for the 45° orientation (approximated by a $\Delta K^{4.5}$ power law) than for the T-L and L-T orientations (approximated by a $\Delta K^{2.6}$ power law). Although the 45° orientation results in a lower fatigue crack growth rate for $\Delta K < 13$ MPa$\sqrt{m}$ than is observed for the T-L and L-T orientations, a greater environmental degradation is also observed.

References

1.Dawson, D. B.; and Pelloux, R.M.: Corrosion Fatigue Crack Growth of Titanium Alloys in Aqueous Environments. *Metallurgical Transactions A*, vol. 5, 1974, pp. 723-731.

2.Bomberger, H.B.; Meyn, D.A.; and Fraker, A.C.: Environmental Effects on Titanium and Its Alloys. *Titanium: Science and Technology V*, Volume 4, G. Lütjering, U. Zwicker and W. Bunk eds., Deutsche Gesellschaft für Metallkunde E.V. Oberursel, 1985, pp. 2435-2454.

3.Sugano, M.; Kanno, S.; and Satake, T.: Fatigue Behavior of Titanium in Vacuum. *Acta Metallurgica*, vol. 37, no. 7, 1989, pp. 1811-1820.

4.Wei, R.P.; and Ritter, D.L.: The Influence of Temperature on Fatigue Crack Growth in a Mill Annealed Ti-6Al-4V Alloy. *Journal of Materials*, vol. 7, no. 2, 1972, pp. 240-250.

5.Peters, M.; Gysler, A.; and Lütjering, G.: Influence of Texture on Fatigue Properties of Ti-6Al-4V. *Metallurgical Transactions A*, vol. 15A, 1984, pp. 1597-1605.

6.Collings, E.W.: *The Physical Metallurgy of Titanium Alloys.* American Society for Metals, 1984, pp. 170-180.

7.ASTM: Standard Test Method for Measurement of Fatigue Crack Growth Rates, E 647-99. *Annual Book of ASTM Standards*, Vol. 03.01, 2000, pp. 591-630.

8.Herman, W.A.; Hertzberg, R.W.; and Jaccard, R.: A Simplified Laboratory Approach for the Prediction of Short Crack Behavior in Engineering Structures. *Fatigue and Fracture of Engineering Materials and Structures*, vol. 11, no. 4, 1988, pp. 303-320.

9.Hertzberg, R.; et al.: Simulation of Short Crack and Other Low Closure Loading Conditions Utilizing Constant K_{max} ΔK-Decreasing Fatigue Crack Growth Procedures. *Small-Crack Test Methods, ASTM STP 1149*, J.M. Larsen, and J.E. Allison, eds., American Society for Testing and Materials, 1992, pp. 197-220.

10. Elber, W.: The Significance of Fatigue Crack Closure. *Damage Tolerance in Aircraft Structures, ASTM STP 486*, ASTM, 1971, pp. 230-242.

11. Elber, W.: *Crack-Closure and Crack Growth Measurements in Surface-Flawed Titanium Alloy Ti-6Al-4V.* NASA TN D-8010, Sep. 1975.

12. Forman, R.G.: *NASAFLAGRO 2.0.*

13. Broek, D.: *Elementary Engineering Fracture Mechanics*, 4th ed., Martinum Nijhoff, 1986, pp. 208-217, 266-272, 321-323.

14. Fanning, J.C.: Timetal®21S Property Data. *Beta Titanium Alloys in the 1990's*, D. Eylon, R.R. Boyer, and D.A. Koss eds., TMS, 1993, pp. 397-410.

15.Newman, J.A.; Riddell, W.T.; and Piascik, R.S.: Effects of K_{max} on Fatigue Crack Growth Threshold in Aluminum Alloys. *Fatigue Crack Growth Thresholds, Endurance Limits, and Design, ASTM STP 1372*, J.C. Newman, Jr. and R.S. Piascik, eds., American Society for Testing and Materials, 1999, pp. 63-77.

16. Riddell, W.T.; and Piascik, R.S.: *Stress Ratio Effects on Crack Opening Loads and Crack Growth Rates in Aluminum Alloy 2024*, NASA/TM-1998-206929, NASA Langley Research Center, 1998.

17. Döker, H.; and Bachmann, V.: Determination of Crack Opening Load by Use of Threshold Behavior. *Mechanics of Fatigue Crack Closure, ASTM STP 982*, J.C. Newman, Jr. and W. Elber, eds., American Society for Testing and Materials, 1988, pp. 247-259.

18. Smith, S.W.; and Piascik, R.S.: An Indirect Technique for Determining Closure-Free Fatigue Crack Growth Behavior. *Fatigue Crack Growth Thresholds, Endurance Limits, and Design, ASTM STP 1372*, J.C. Newman, Jr. and R.S. Piascik, eds., American Society for Testing and Materials, 1999, pp. 109-122.

19. Wei, R.P.: Fatigue-Crack Propagation in a High-Strength Aluminum Alloy. *International Journal of Fracture Mechanics*, vol. 4, no. 2 , 1968, pp. 159-168.

20. Wei, R.P.: Some Aspects of Environment-Enhanced Fatigue-Crack Growth. *Engineering Fracture Mechanics*, vol. 1, 1970, pp. 633-651.

21. Pao, P.S.; and Wei, R.P.: Hydrogen-Enhanced Fatigue Crack Growth in Ti-6Al-2Sn-4Zr-2Mo-0.1Si. *Titanium: Science and Technology V*, Volume 4. G. Lütjering, U. Zwicker and W. Bunk eds., Deutsche Gesellschaft für Metallkunde E.V. Oberursel, 1985, pp. 2503-2510.

22. Evans, W.J.; and Gostelow, C.R.: The Effect of Hold Time on the Fatigue Properties of a β-Processed Titanium Alloy. *Metallurgical Transactions A*, vol. 10A, 1979, pp. 1837-1846.

23. Bowen, A.W.: Fatigue Crack Growth in Strongly Textured Ti-6Al-4V. *Texture and the Properties of Materials.* G.J. Davies et al. eds., The Metals Society, 1976, pp. 218-223.

24. Bowen, A.W.: The Influence of Crystallographic Orientation on the Fracture Toughness of Strongly Textured Ti-6Al-4V. *Acta Metallurgica*, vol. 26, 1978, pp. 1423-1433.

25. Fuggle, J.C.; Watson, L.M.; Fabian, D.J.; and Affrossman, S.: X-Ray Photoelectron Studies of the Reaction of Clean Metals (Mg, Al, Cr, Mn) with Oxygen and Water Vapor. *Surface Science*, vol. 49, 1975, pp. 61-76.

26. Padalia, B.D.; Gimzewski, J.K.; Affrossman, S.; Lang, W.C.; Watson, L.M.; and Fabian, D.J.: The Reactions of Oxygen and Water with the Rare-Earth Metals Terbium to Lutetium Studied by X-Ray Photoelectron Spectroscopy. *Surface Science*, vol. 61, 1976, pp. 468-482.

27. Gregory, J.K.: Fatigue Crack Propagation in Titanium Alloys. *Handbook of Fatigue Crack Propagation in Metallic Structures*, A. Carpinteri ed., Elsevier Science, 1994, pp. 281-322.

28. Piascik, R.S.; and Newman, J.C., Jr.: An Extended Compact Tension Specimen for Fatigue Crack Growth and Fracture Testing. *International Journal of Fracture*, vol. 76, 1995, pp. R43-R48.

Table I. Material Chemistry, wt. %.

Alloy	Al	Zr	Cr	Sn	Mo	Nb	V	Fe	Si	O
Ti 6-2-2-2-2[#]	5.60	1.81	1.79	1.88	1.96	---	---	0.03	0.23	0.103
Timetal 21S	3.00	---	---	---	14.95	2.62	---	0.34	0.195	0.145
Ti 6Al-4V[*]	6.3	---	---	---	---	---	4.0	0.15	---	0.16

- Beta Transus: 960 ± 6°C (1760 ± 10°F)
* - Nominal Composition

Table II. Microstructure of Three Ti Sheet Products.

Alloy	Grain size	Volume fraction β	Morphology
Ti 6-2-2-2-2	< 10 μm	35 - 45 %	Primary α and transformed β colonies
Timetal 21S	25 - 50 μm	70 - 80 %	Grain boundary α and platelet α in retained β
Ti 6Al-4V	< 15 μm	10 - 20 %	α matrix with grain boundary β

Table III. Mechanical Properties.

Alloy	Tensile axis	σ_{UTS} (MPa)	σ_{ys} (MPa) (0.2% offset)	E (GPa)
Ti 6-2-2-2-2	L	1161.1	1121.8	116.5
	T	1145.2	1110.7	121.9
Timetal 21S	L	1299.7	1196.2	---
	T	1320.3	1241.1	104.1
Ti 6Al-4V	L	986.6	901.1	113.1
	T	----	----	109.6

Table IV. Threshold Test Results for T-L Oriented Ti 6-2-2-2-2 Specimens at 24 °C (from Fig. 7).

Fatigue Crack Growth Test	ΔK_{th} (MPa$\sqrt{m}$)	R at Threshold	K_{max} at Threshold (MPa$\sqrt{m}$)
Constant R	2.81	0.10	3.12
Constant R	2.09	0.50	4.18
Constant K_{max}	1.94	0.49	3.85
Constant K_{max}	1.53	0.77	6.60
Constant K_{max}	1.61	0.85	11.0
Constant K_{max}	1.52	0.91	16.5
Constant K_{max}	1.41	0.94	22.0

Table V. Threshold Test Results for T-L Oriented Ti 6-2-2-2-2 Specimens at 177 °C (from Fig. 14).

Fatigue Crack Growth Test	ΔK_{th} (MPa$\sqrt{m}$)	R at Threshold	K_{max} at Threshold (MPa$\sqrt{m}$)
Constant R	3.11	0.10	3.46
Constant R	2.22	0.50	4.44
Constant K_{max}	1.65	0.90	16.5
Constant K_{max}	1.50	0.93	22.0
Constant K_{max}	1.39	0.97	44.0

Table VI. Threshold Test Results for L-T Oriented Ti 6-2-2-2-2 Specimens at 24 °C (from Fig. 19).

Fatigue Crack Growth Test	ΔK_{th} (MPa$\sqrt{m}$)	R at Threshold	K_{max} at Threshold (MPa$\sqrt{m}$)
Constant R	2.79	0.10	3.10
Constant R	2.10	0.50	4.20
Constant K_{max}	1.55	0.90	16.5
Constant K_{max}	1.49	0.93	22.0
Constant K_{max}	1.46	0.97	33.0

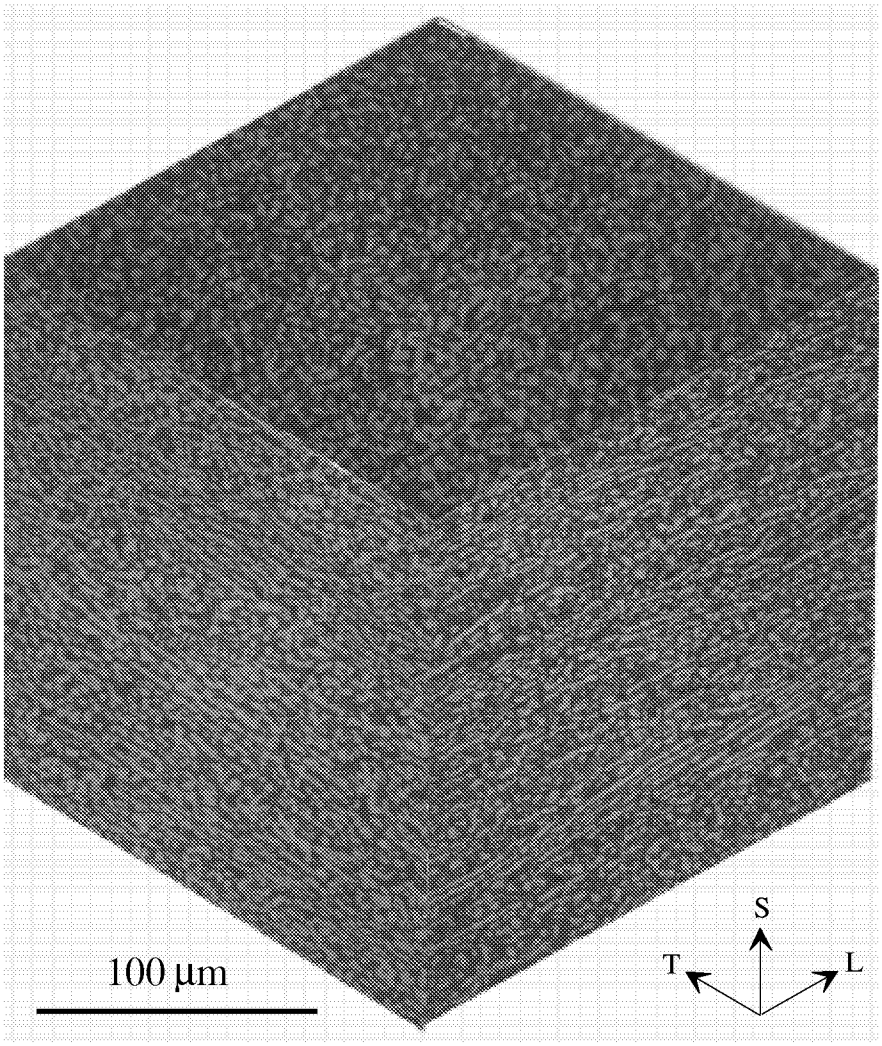

Figure 1. Composite optical micrograph of Ti 6-2-2-2-2-2 sheet product. Primary α grains appear light in the micrograph, while transformed β grains are dark.

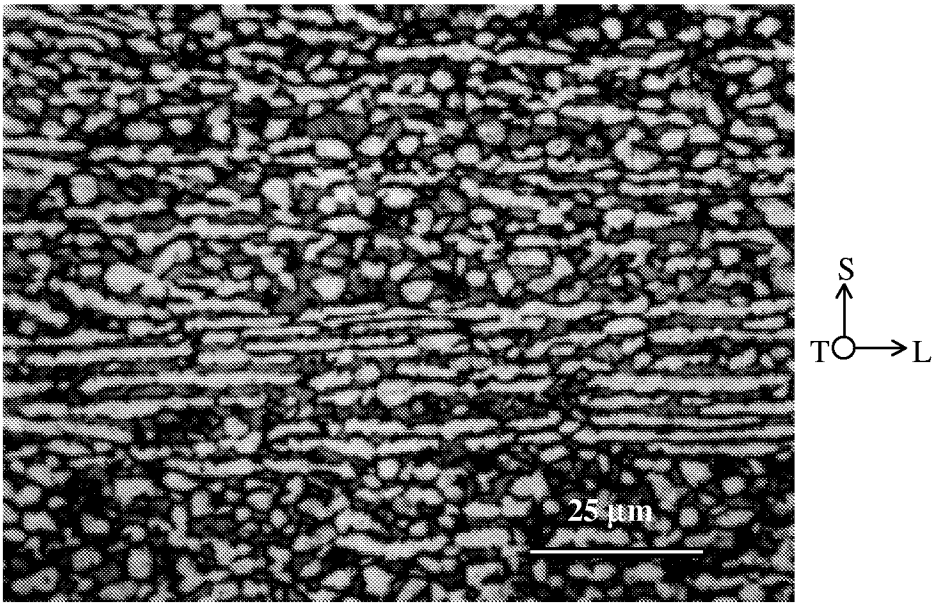

Figure 2. Optical micrograph of the cross rolled Ti 6-2-2-2-2 sheet, normal to long transverse direction. Primary α grains appear light in the micrograph, while transformed β grains are dark.

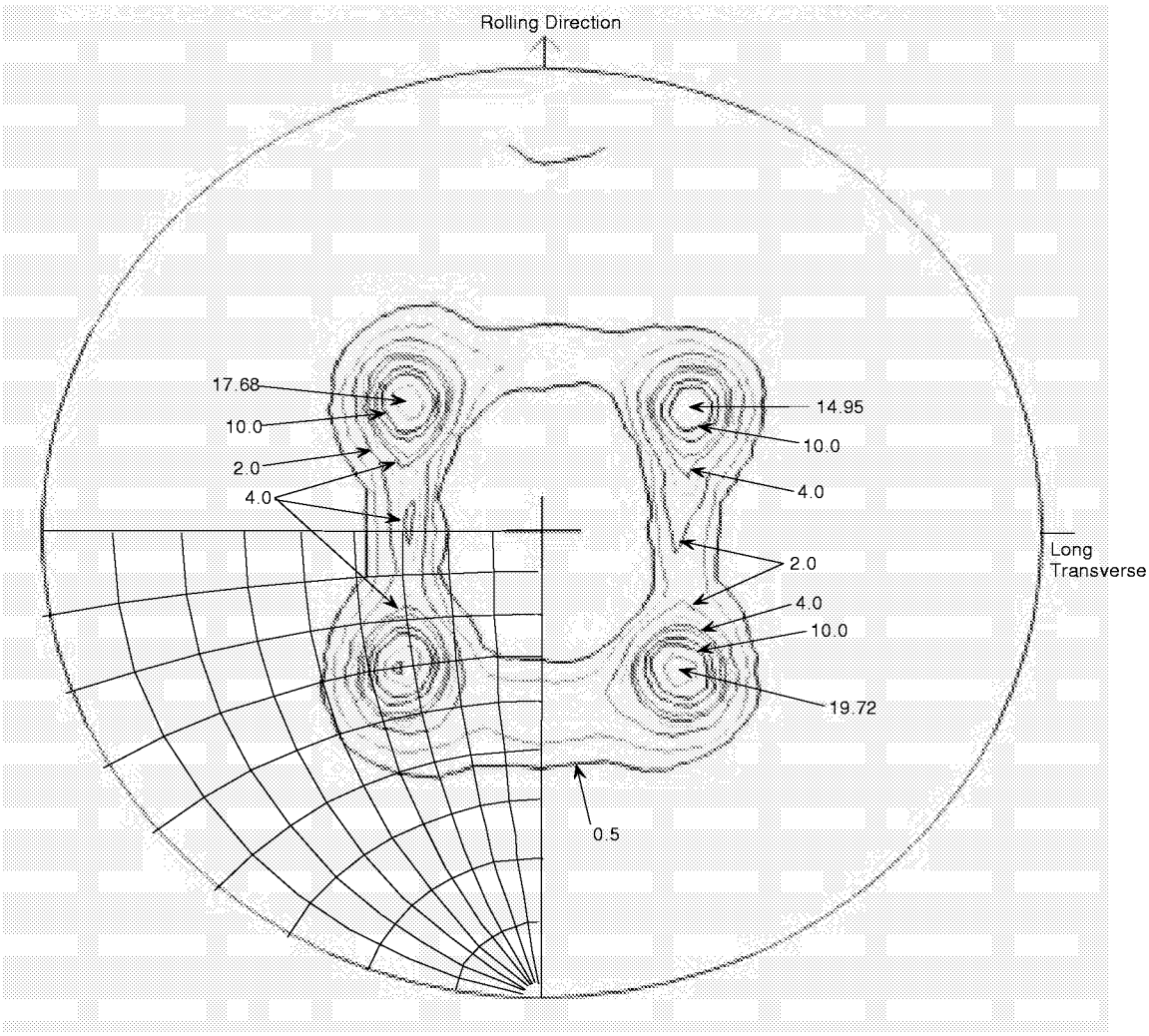

Figure 3. Basal plane (0002) pole figure for Ti 6-2-2-2-2 sheet, examined at the t/4 plane. Included in the lower left quadrant is a stereographic projection drawn with 10° intervals.

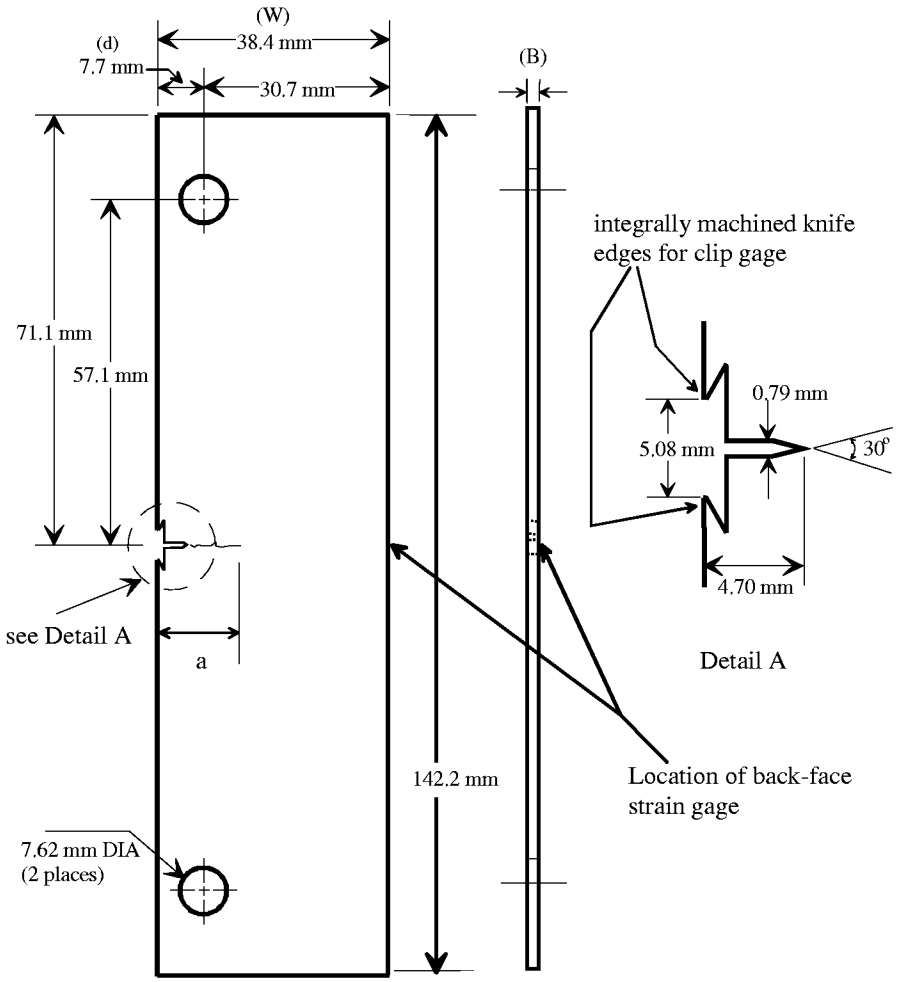

Figure 4. Specimen design for eccentrically loaded single edge notch tensile (ESE(T)) specimen.

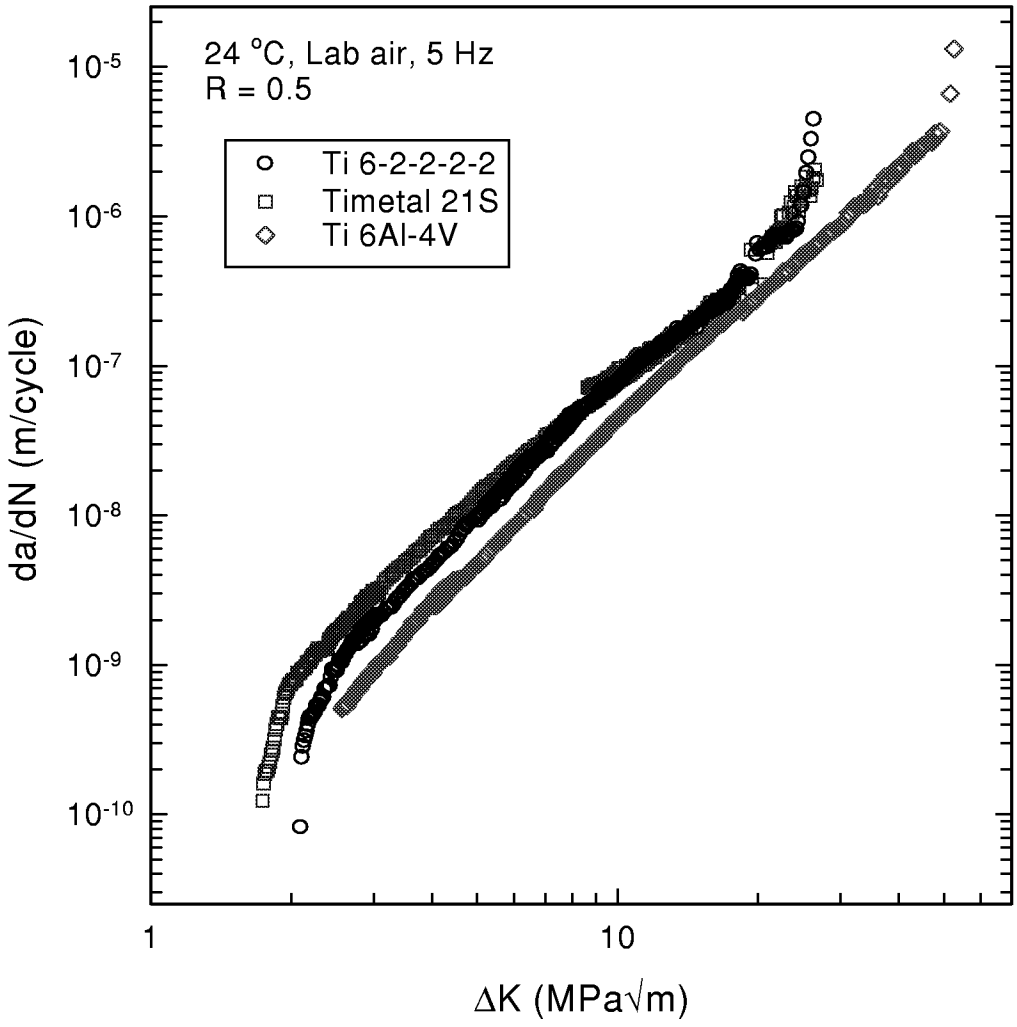

Figure 5a. Fatigue crack growth rate versus cyclic stress-intensity factor for T-L oriented Ti 6-2-2-2-2, Timetal 21S, and Ti 6Al-4V tested in room temperature laboratory air at 5 Hz and R = 0.5.

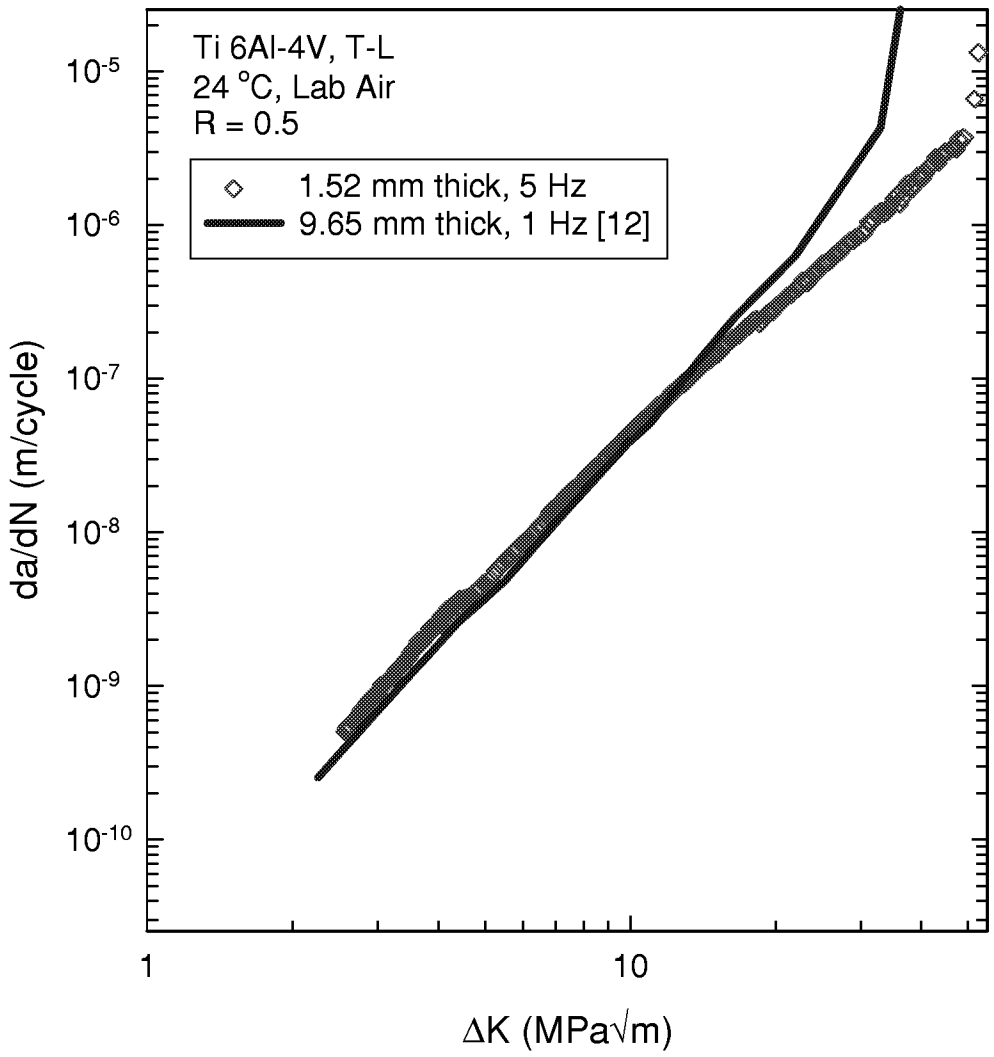

Figure 5b. Fatigue crack growth rate versus cyclic stress-intensity factor for T-L oriented Ti 6Al-4V tested in room temperature laboratory air at R = 0.5.

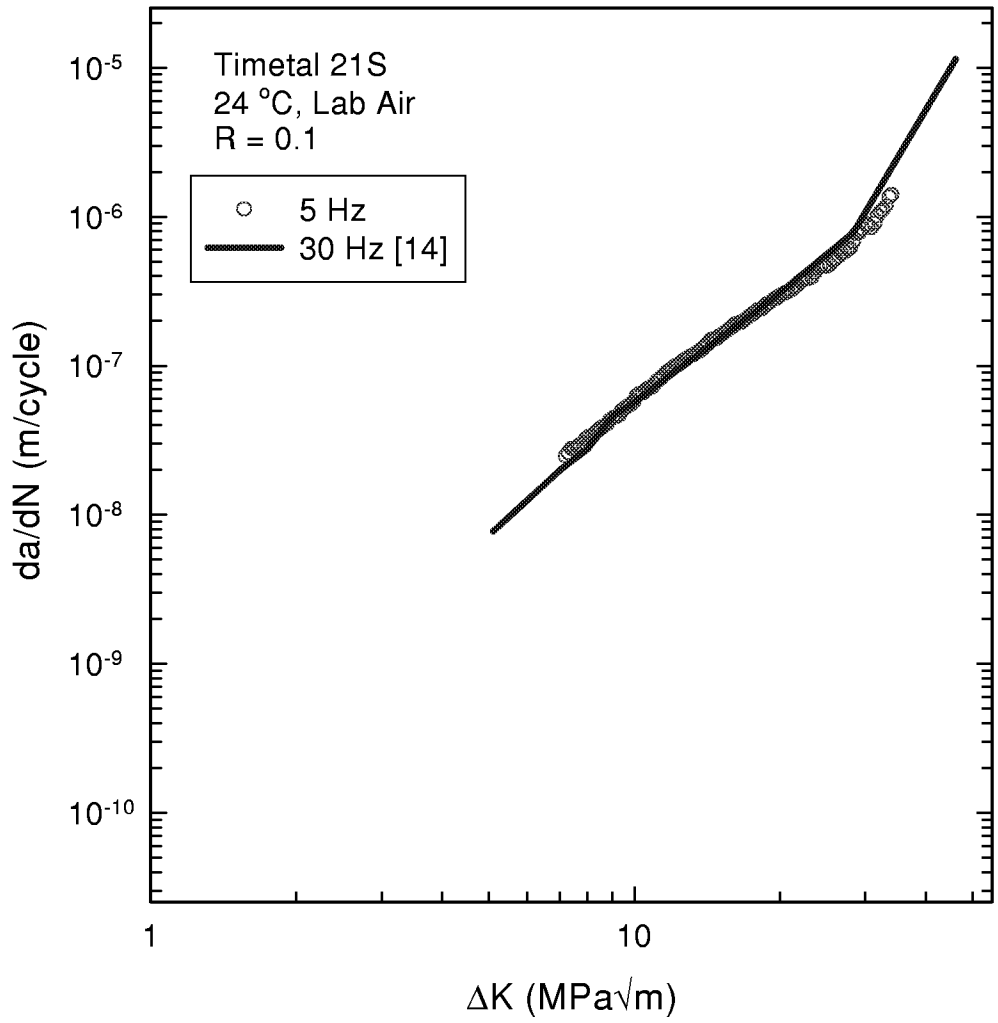

Figure 5c. Fatigue crack growth rate versus cyclic stress-intensity factor for Timetal 21S tested in room temperature laboratory air at R = 0.1.

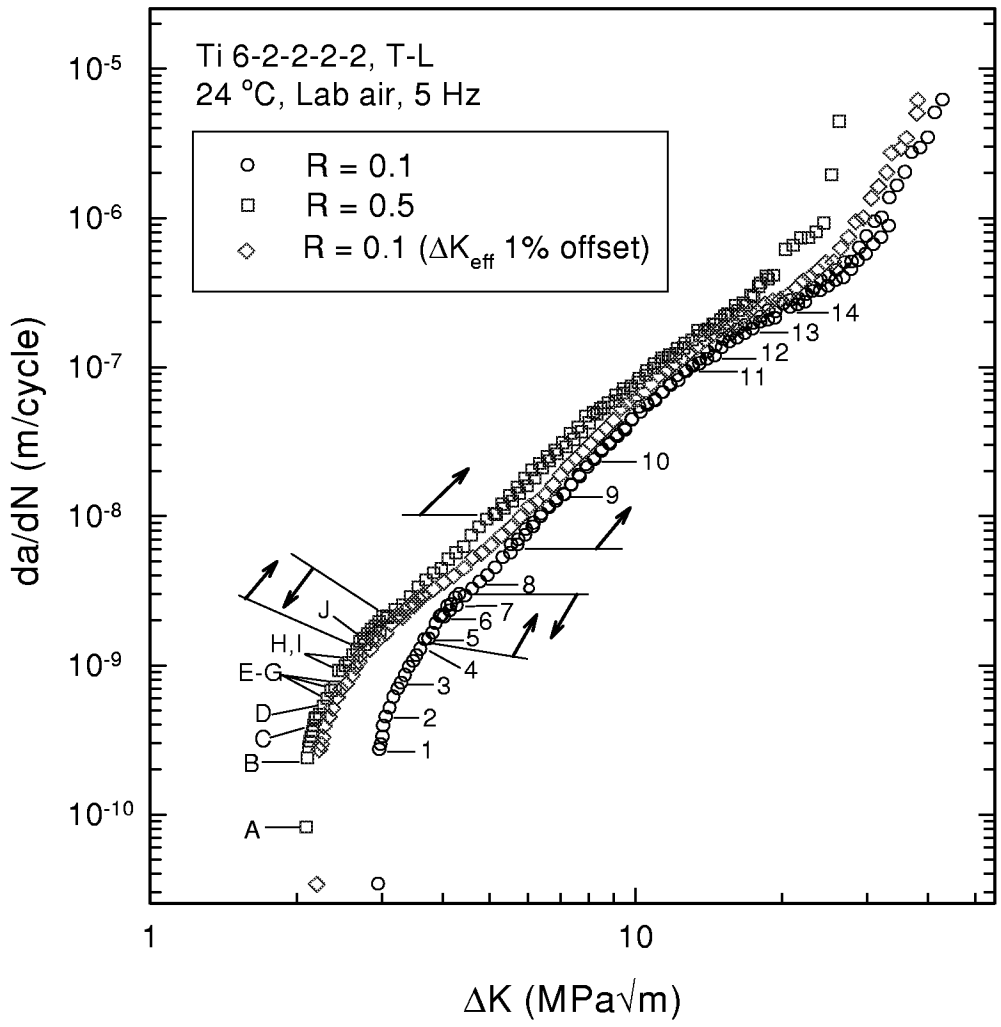

Figure 6. Fatigue crack growth rates for Ti 6-2-2-2-2, T-L orientation, in room temperature laboratory air at 5 Hz. Numbers and letters indicate load-displacements measurements to determine opening loads. Three test were performed at each R and the starting point and direction of tests (K-increasing or K-decreasing) are noted with arrows.

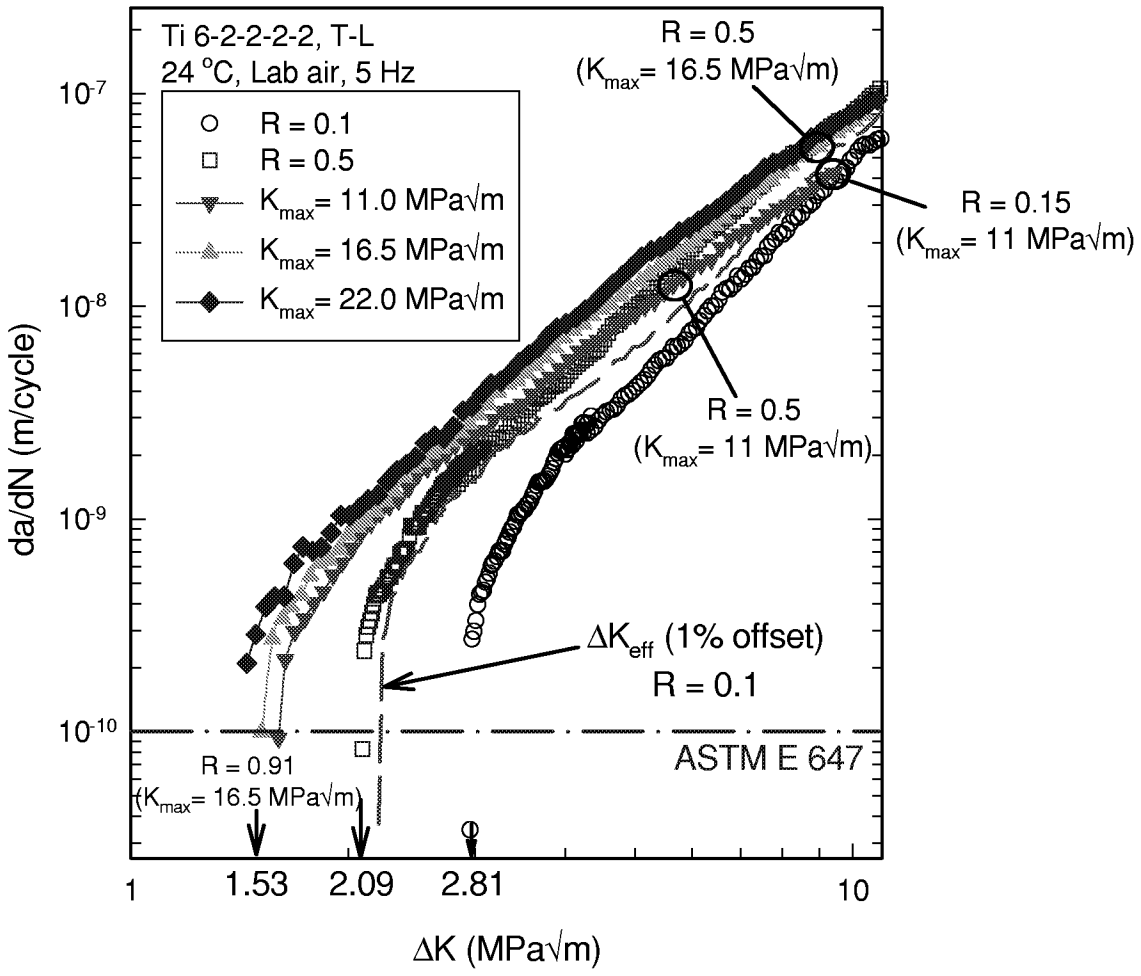

Figure 7. Lower Paris to threshold regime fatigue crack growth rates for Ti 6-2-2-2-2, T-L orientation, for constant-R and constant-K_{max} testing in room temperature laboratory air. Noted in the figure are regions of correlation (similar R) between the different types of tests.

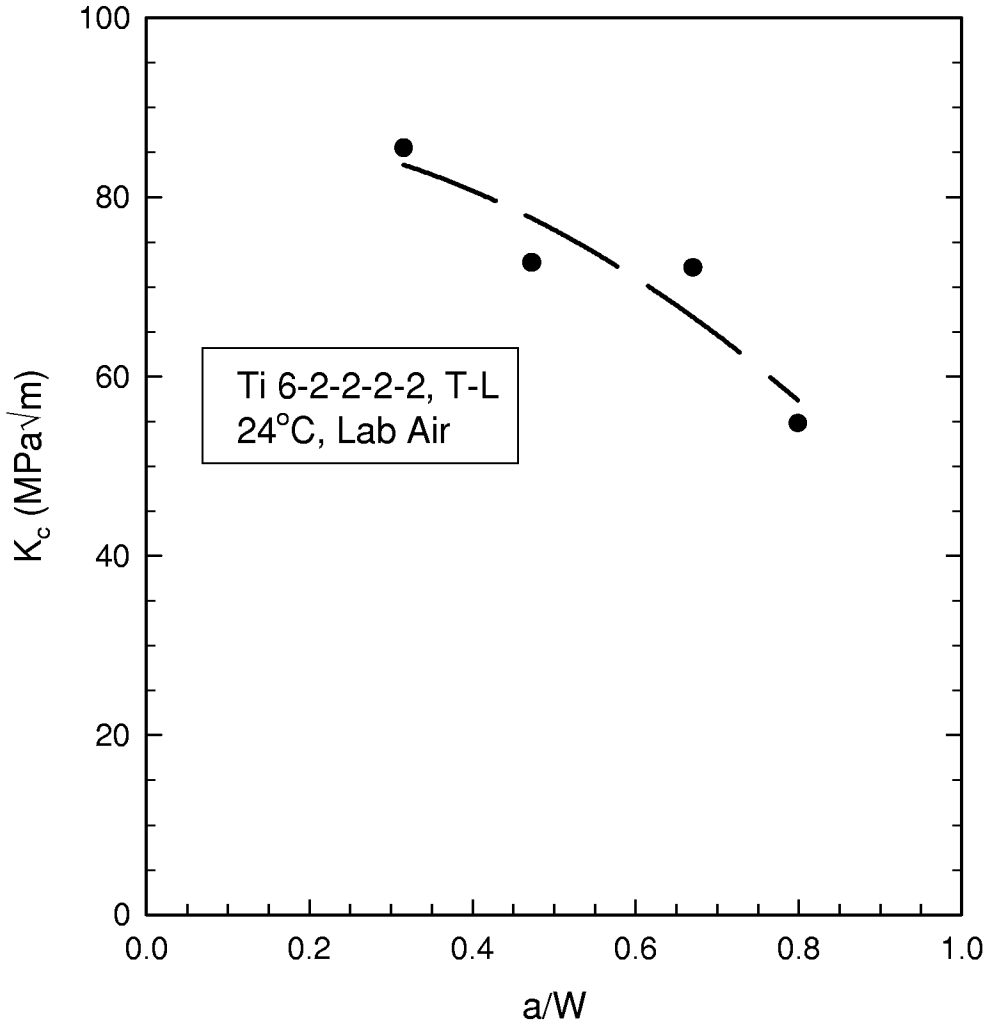

Figure 8. Apparent fracture toughness (K_c) versus a/W for Ti 6-2-2-2-2-2, T-L orientation, in room temperature laboratory air.

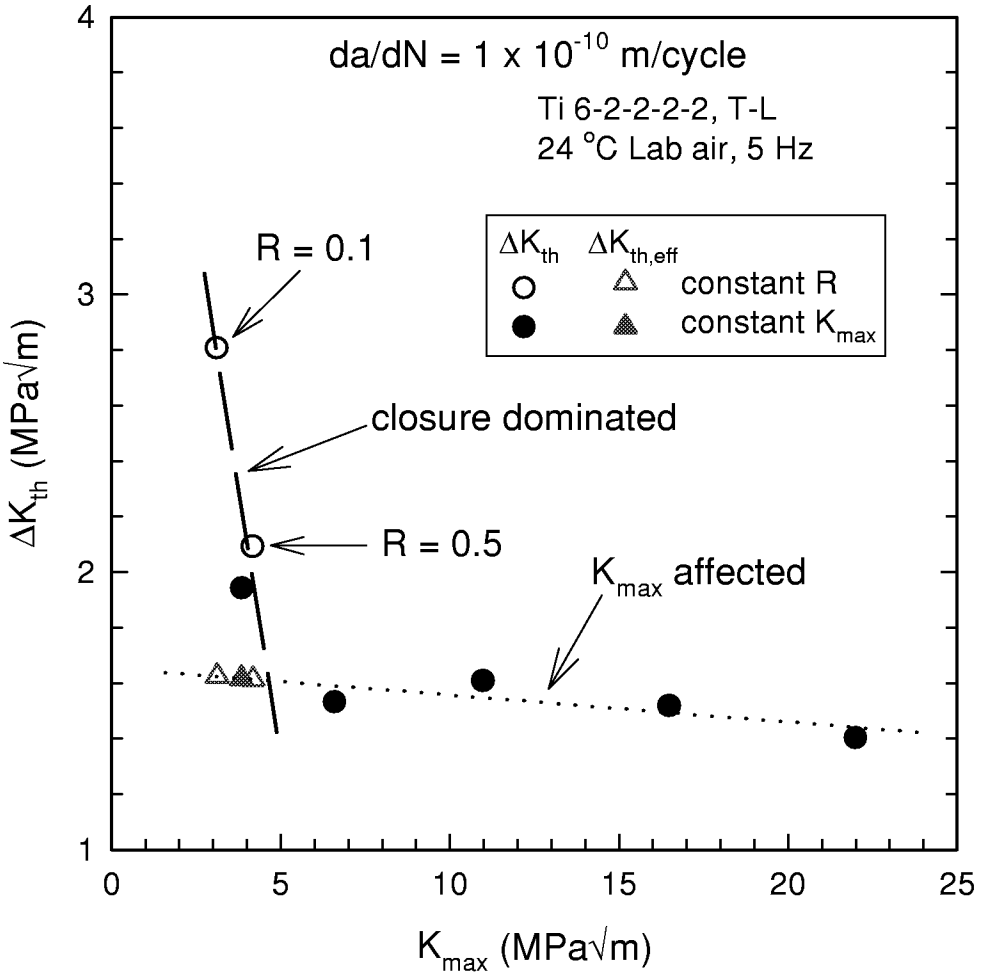

Figure 9. ΔK_{th} versus K_{max} data at 1 x 10^{-10} m/cycle for Ti 6-2-2-2-2, T-L orientation, in room temperature laboratory air. Two distinct regions, a closure-dominated region (dashed line) and a K_{max}-affected region (dotted line) are identified.

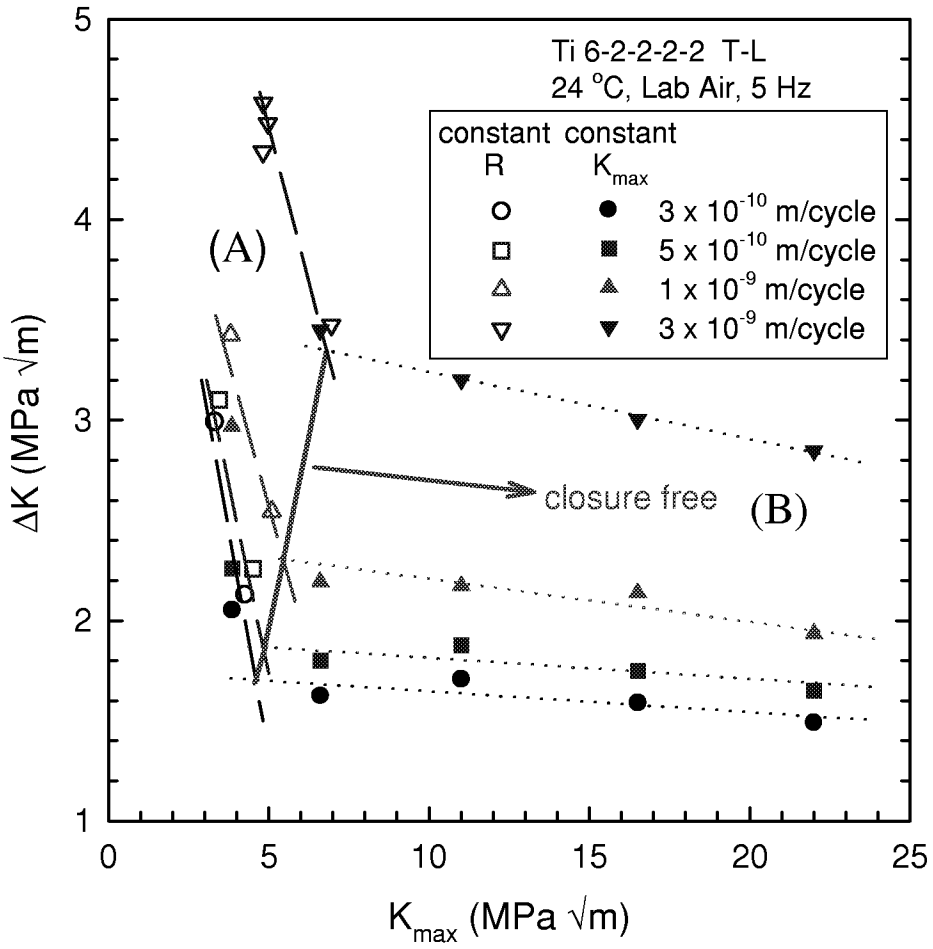

Figure 10. ΔK versus K_{max} data for Ti 6-2-2-2-2, T-L orientation, in room temperature laboratory air at four fatigue crack growth rates. Two distinct regions, a closure-dominated region (A, dashed lines) and a K_{max}-affected region (B, dotted lines) are identified.

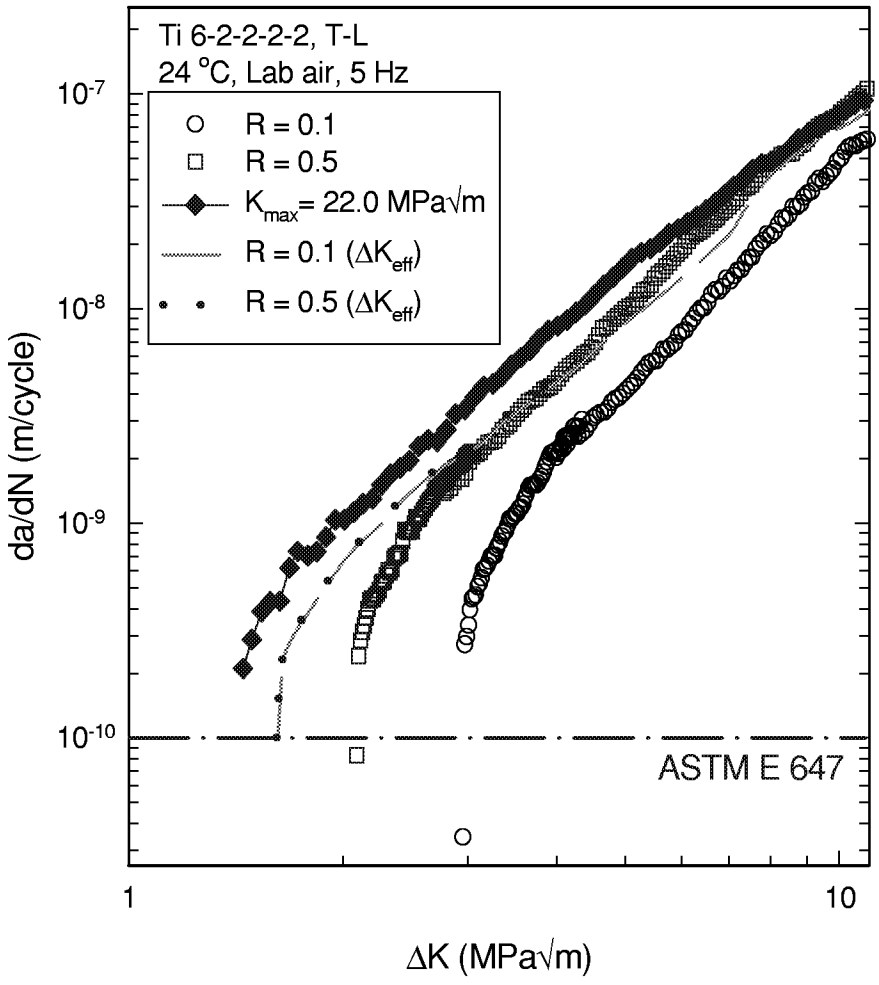

Figure 11. Lower Paris to threshold regime fatigue crack growth rate data for Ti 6-2-2-2-2, T-L orientation, in room temperature laboratory air. ΔK_{eff} curves for R = 0.1 and 0.5 are determined using the ΔK versus K_{max} data.

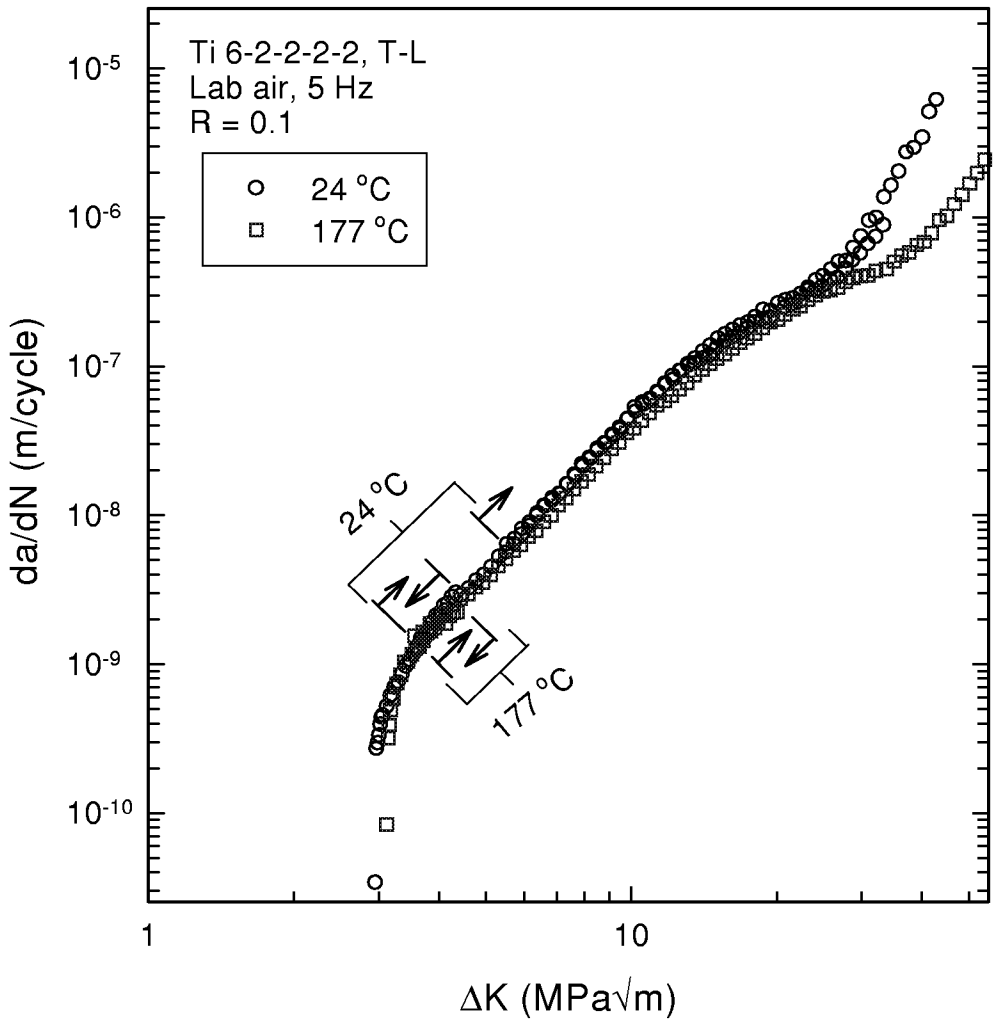

Figure 12. Fatigue crack growth rates for Ti 6-2-2-2-2, T-L orientation, in room and elevated temperature laboratory air, R = 0.1. The starting point and direction of each test (K-increasing or K-decreasing) are noted with arrows.

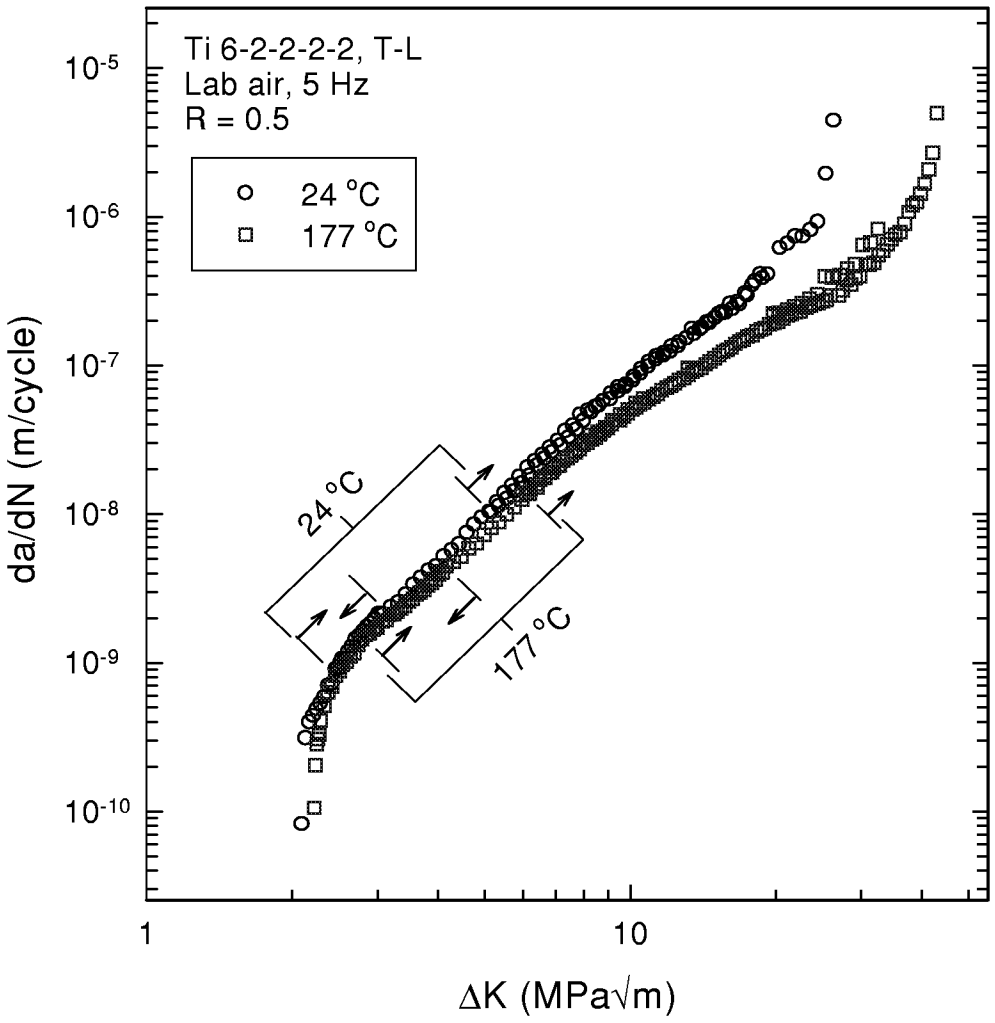

Figure 13. Fatigue crack growth rates for Ti 6-2-2-2-2, T-L orientation, in room and elevated temperature laboratory air, R = 0.5. The starting point and direction of each test (K-increasing or K-decreasing) are noted with arrows.

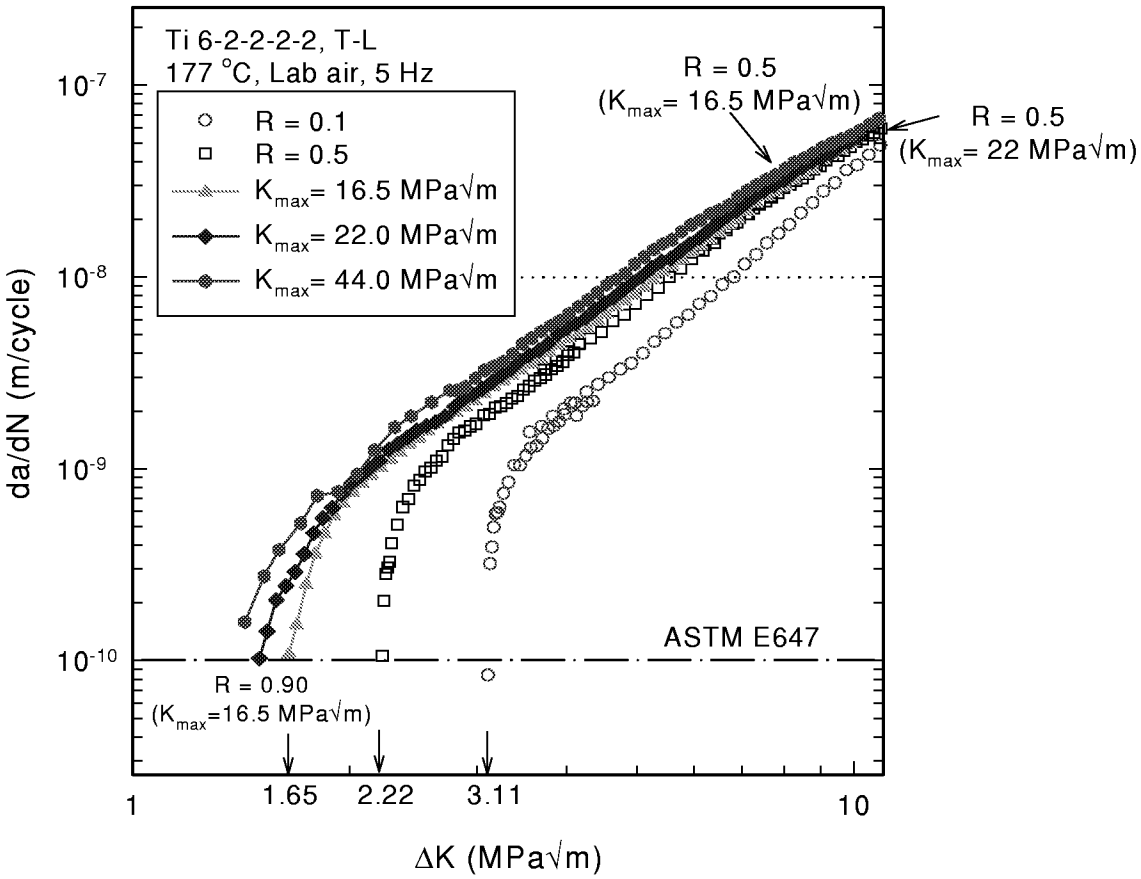

Figure 14. Lower Paris to threshold regime fatigue crack growth rates for Ti 6-2-2-2-2, T-L orientation, constant-R and constant-K_{max} testing in elevated temperature laboratory air. Regions of similar R for the two different test types are noted.

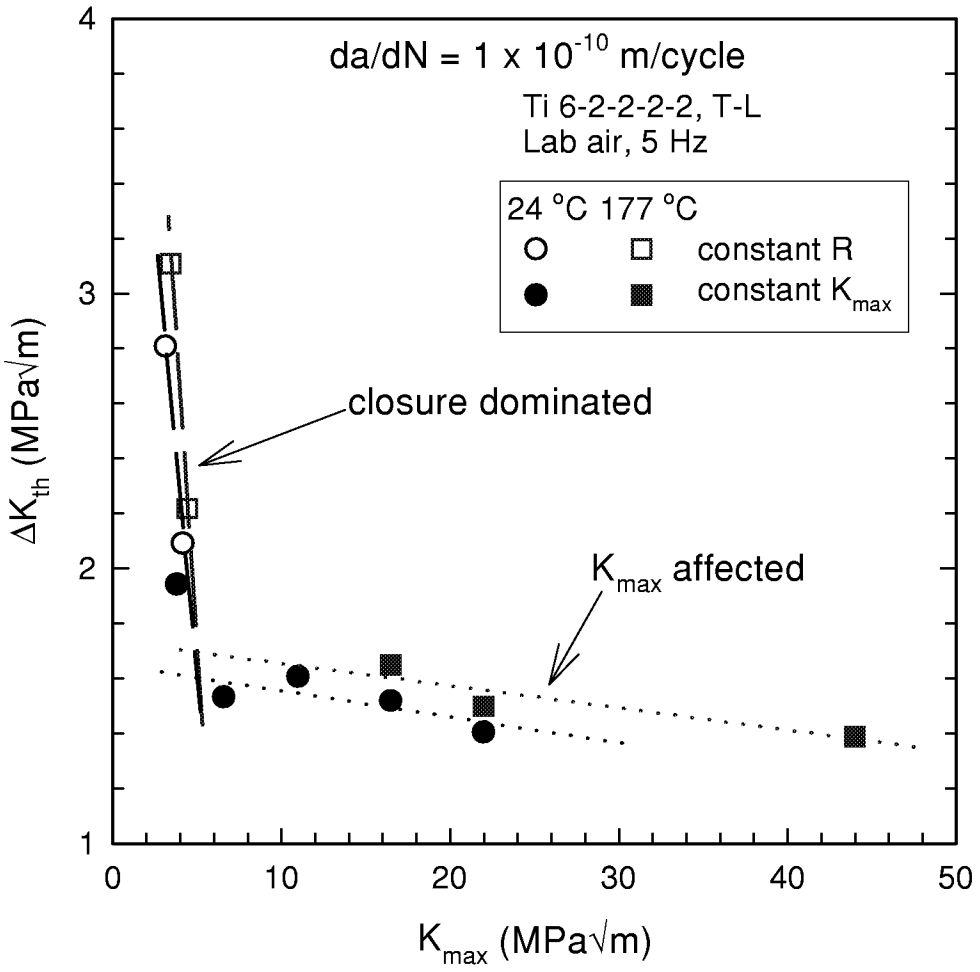

Figure 15. ΔK_{th} versus K_{max} for Ti 6-2-2-2-2 at da/dN = 1 x 10^{-10} m/cycle, T-L orientation, for constant-R and constant-K_{max} testing in room and elevated temperature laboratory air. The data shows two distinct regions, a closure-dominated region (dashed lines) and a K_{max}-affected region (dotted lines).

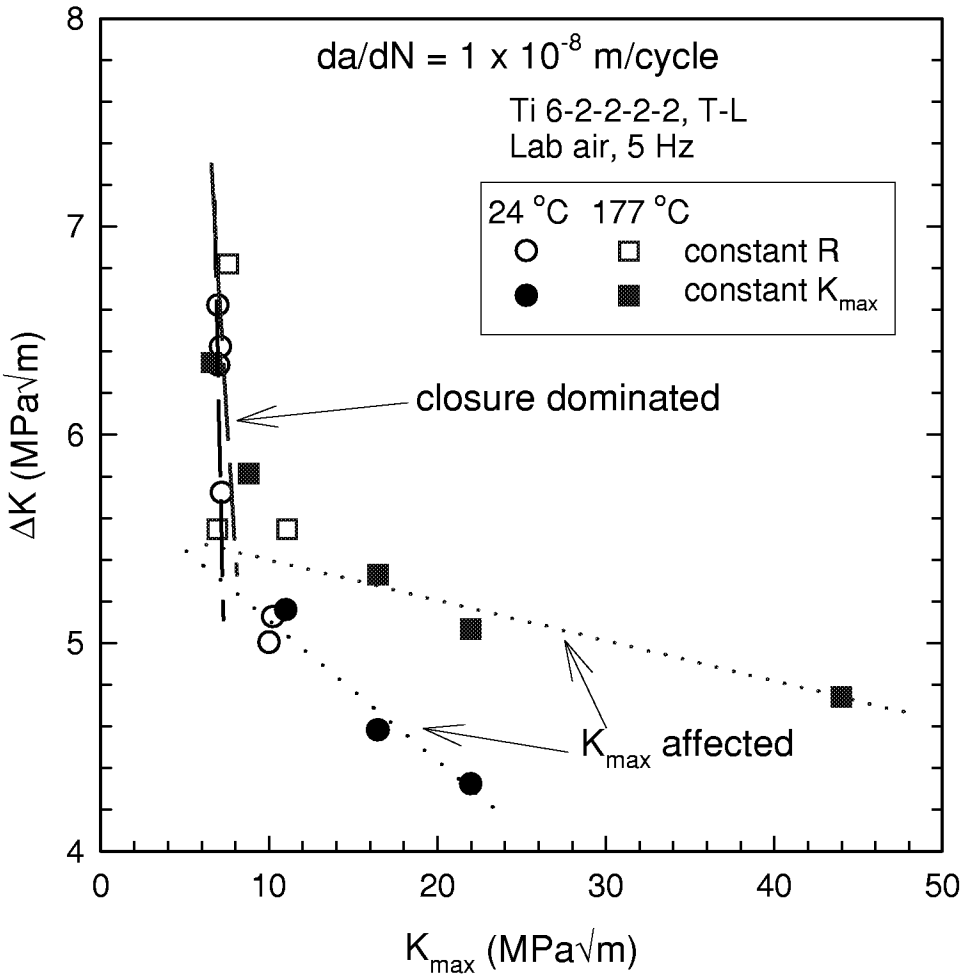

Figure 16. ΔK versus K_{max} for Ti 6-2-2-2-2-2 at da/dN=1 x 10^{-8} m/cycle, T-L orientation, for constant-R and constant-K_{max} testing in room and elevated temperature laboratory air. The data shows two distinct regions, a closure-dominated region (dashed lines) and a K_{max}-affected region (dotted lines).

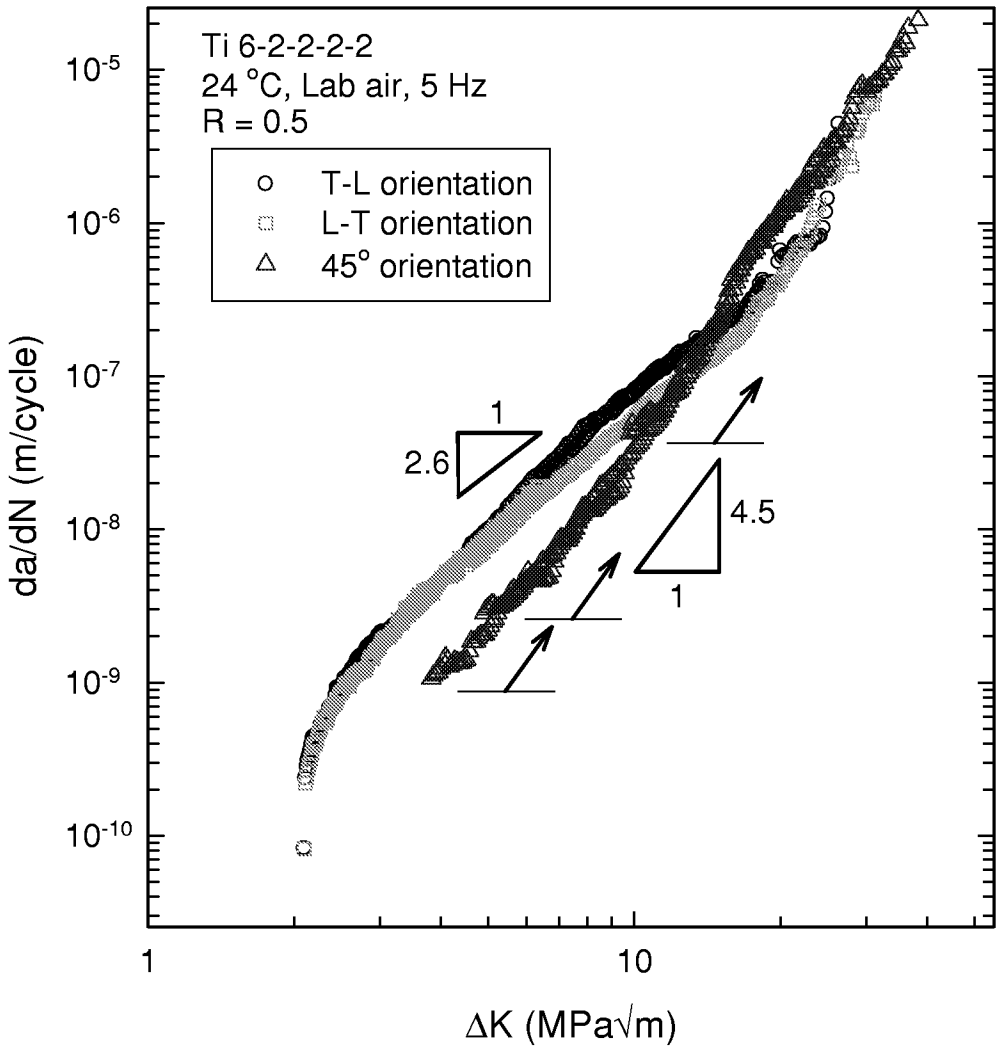

Figure 17. Fatigue crack growth rates for T-L, L-T, and 45° oriented Ti 6-2-2-2-2 in room temperature laboratory air at R = 0.5. Three tests are shown for each orientation. The beginning of each K-increasing test for the 45° orientation is indicated with an arrow. The approximate power law slope in the Paris regime for each orientation is indicated on the plot.

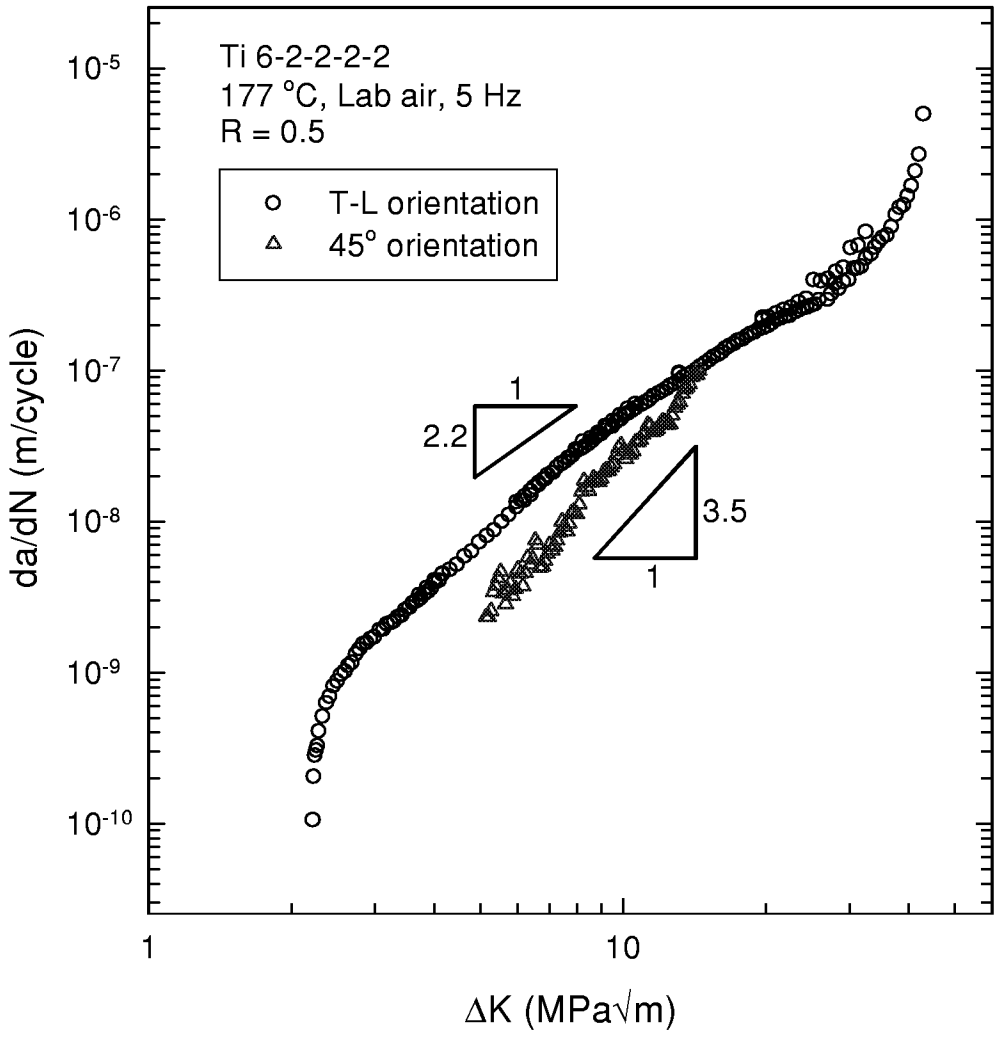

Figure 18. Fatigue crack growth rates for T-L and 45° oriented Ti 6-2-2-2-2 in 177 °C laboratory air at R = 0.5. The approximate power law slope in the Paris regime for each orientation is indicated on the plot.

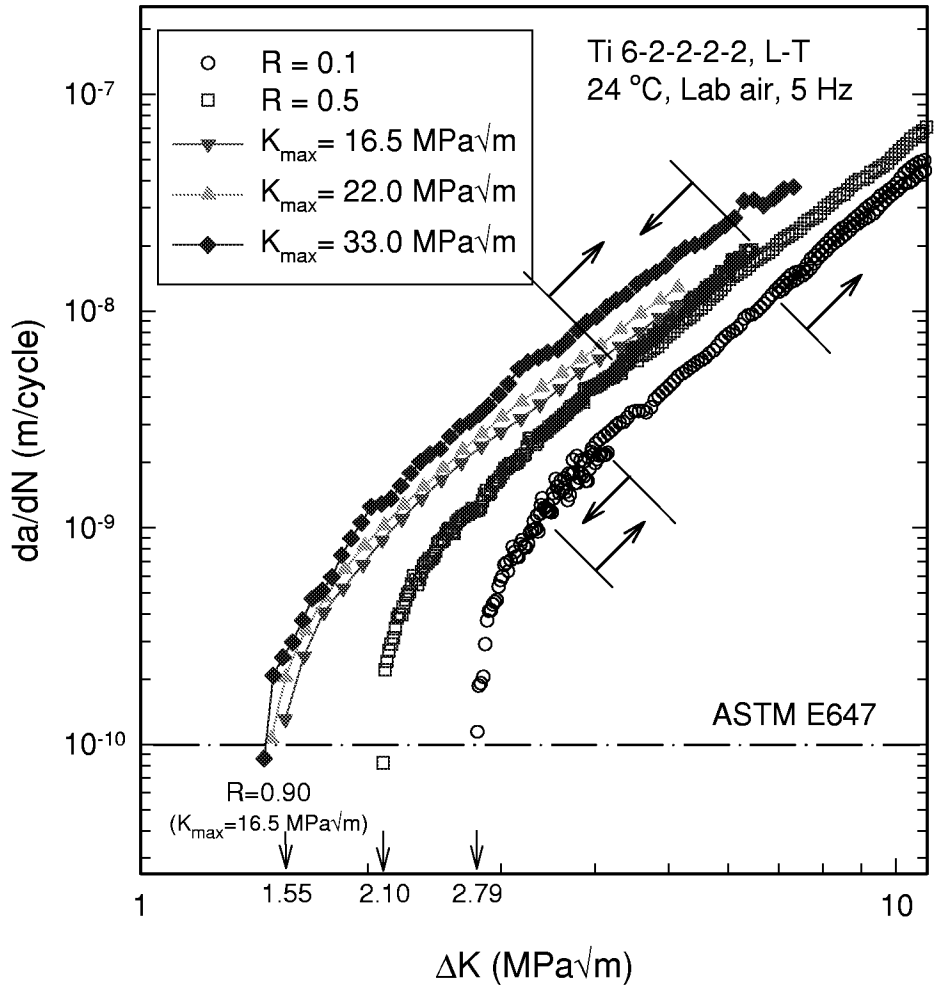

Figure 19. Lower Paris to threshold regime fatigue crack growth rates for Ti 6-2-2-2-2, L-T orientation, for constant-R and constant-K_{max} testing in room temperature laboratory air. The starting point and direction (K-increasing or K-decreasing) of each constant-R test included in this plot is noted with an arrow.

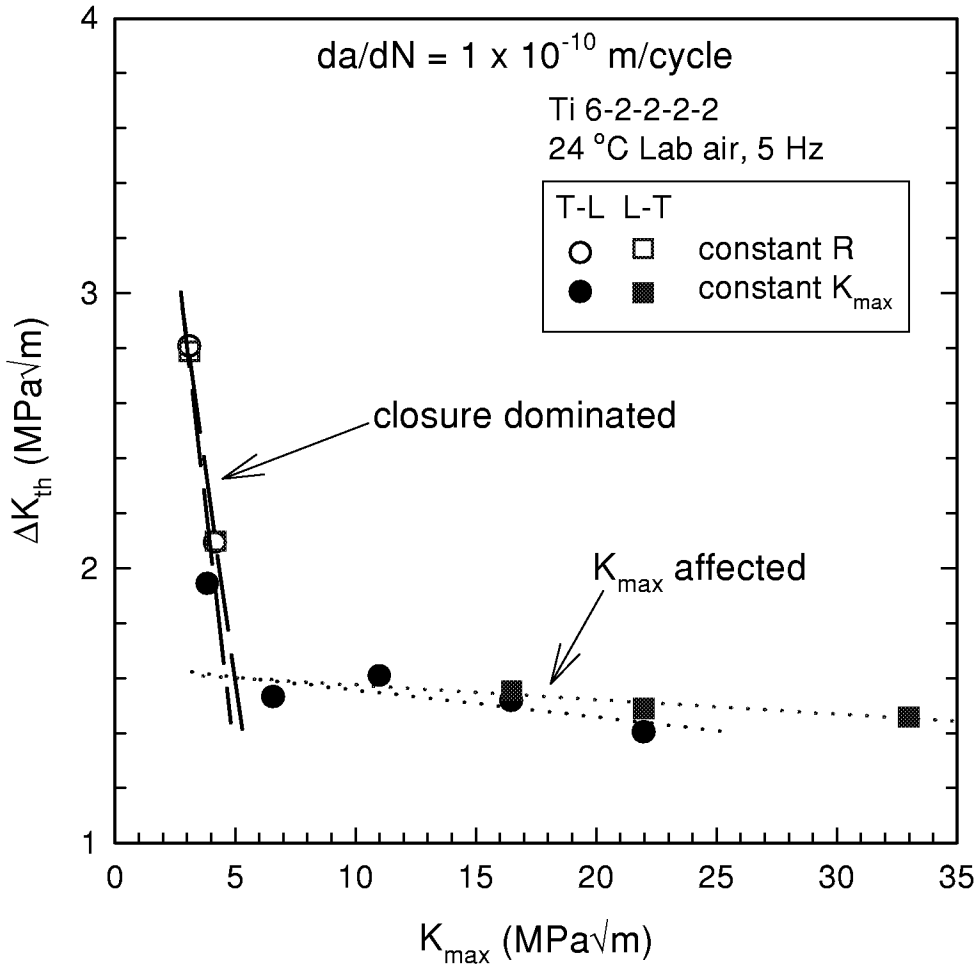

Figure 20. ΔK_{th} versus K_{max} for Ti 6-2-2-2-2 at da/dN = 1 x 10^{-10} m/cycle, T-L and L-T orientations, for constant-R and constant-K_{max} testing in room temperature laboratory air. The data shows two distinct regions, a closure-dominated region (dashed lines) and a K_{max}-affected region (dotted lines).

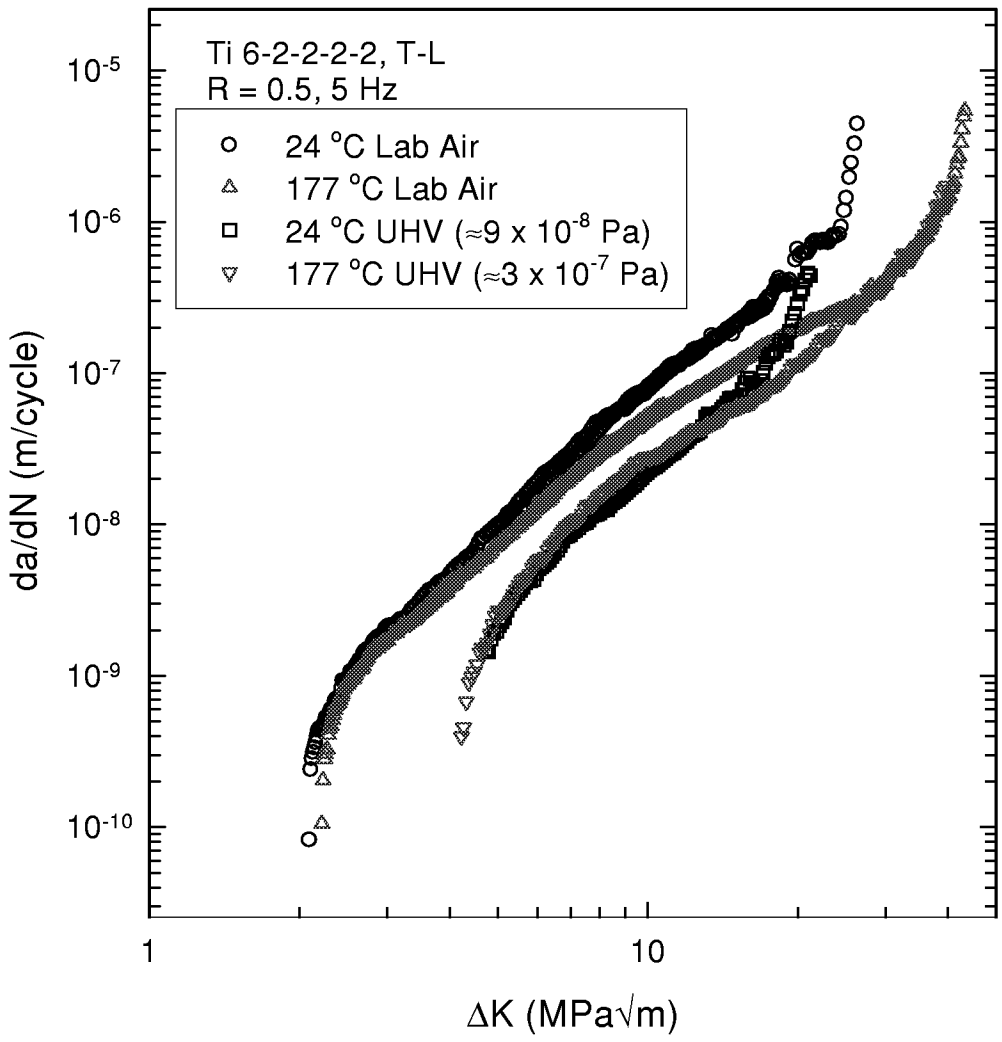

Figure 21. Fatigue crack growth rates for T-L oriented Ti 6-2-2-2-2 tested in laboratory air and ultrahigh vacuum at 24°C and 177°C for R = 0.5.

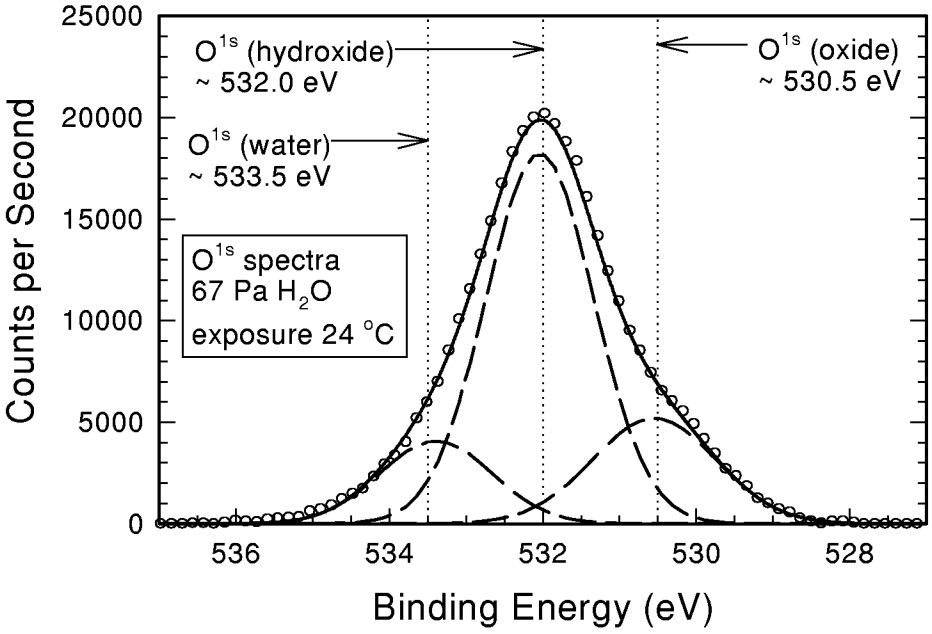

a) room temperature

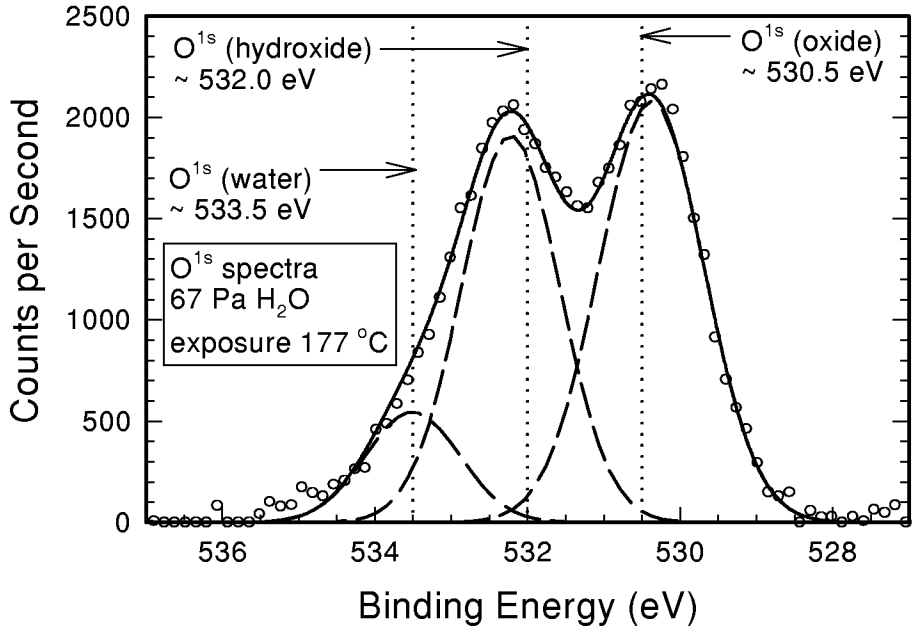

b) 177 °C

Figure 22. XPS spectra from Ti 6-2-2-2-2 fatigue surfaces produced during exposure to 67 Pa water vapor at a) 24°C and b) 177 °C. Constituent peaks are shown as dashed lines and the binding energy of O^{1s} photoelectrons for three compounds are identified by dotted lines.

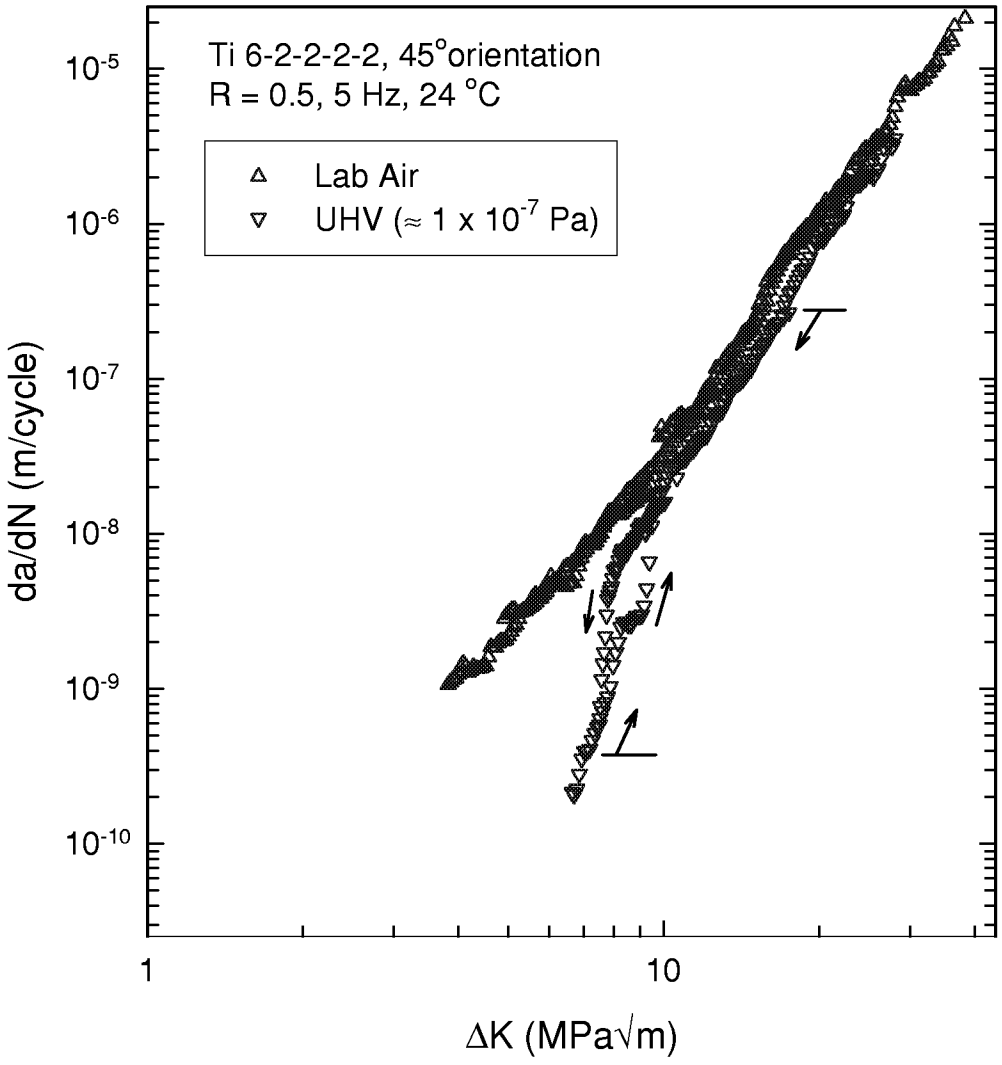

Figure 23. Fatigue crack growth rates for 45° oriented Ti 6-2-2-2-2 tested in room temperature laboratory air and ultrahigh vacuum at R = 0.5.

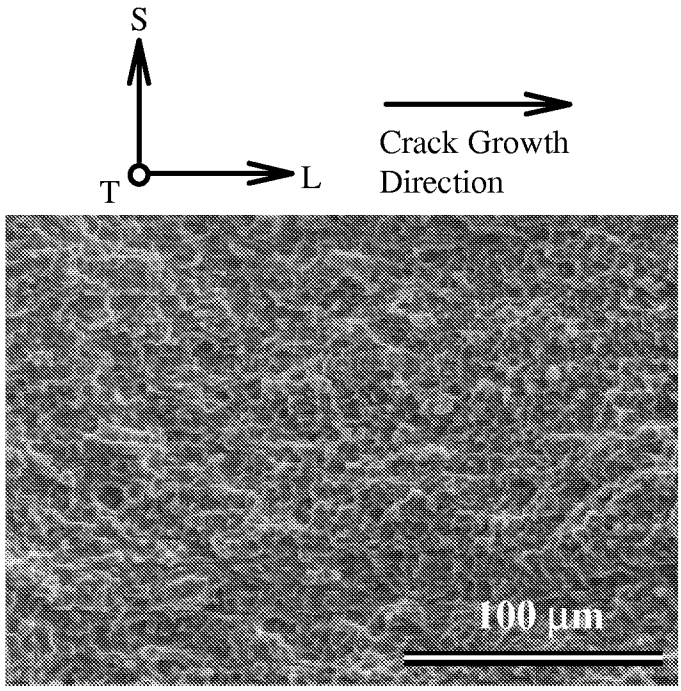

a) room temperature

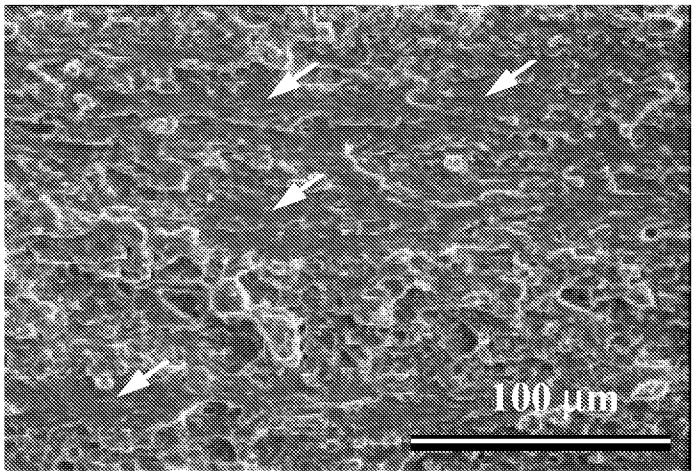

b) 177 °C

Figure 24. SEM micrographs of fatigue surface of Ti 6-2-2-2-2, T-L orientation, ΔK = 19.8 MPa$\sqrt{m}$, R = 0.5 tested at a) 24 °C and b) 177 °C in laboratory air.

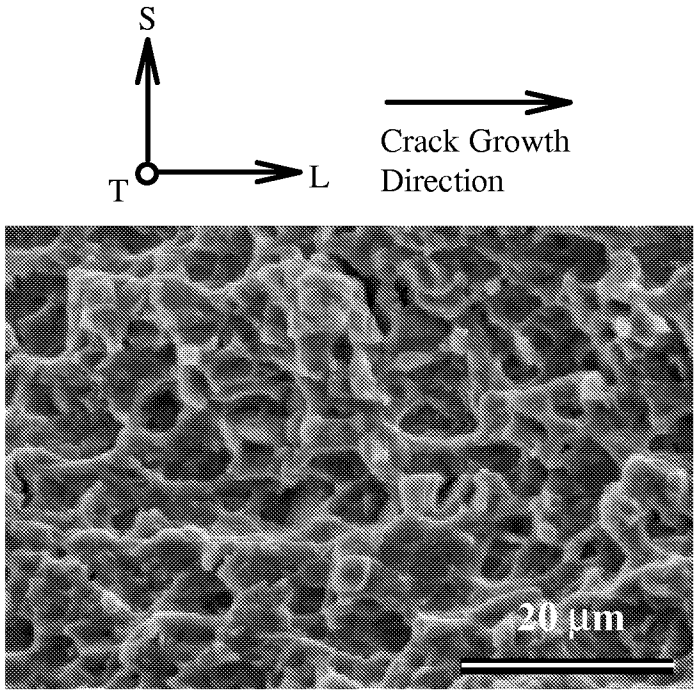

a) room temperature

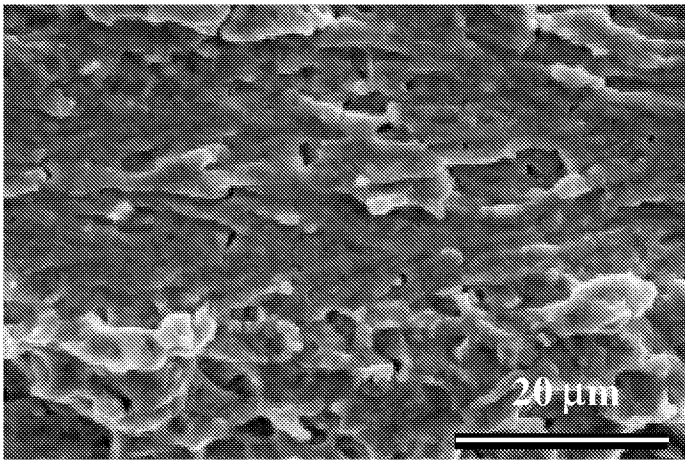

b) 177 °C

Figure 25. SEM micrographs of fatigue surface of Ti 6-2-2-2-2, T-L orientation, $\Delta K = 19.8$ MPa$\sqrt{m}$, $R = 0.5$ tested at a) 24 °C and b) 177 °C in laboratory air.

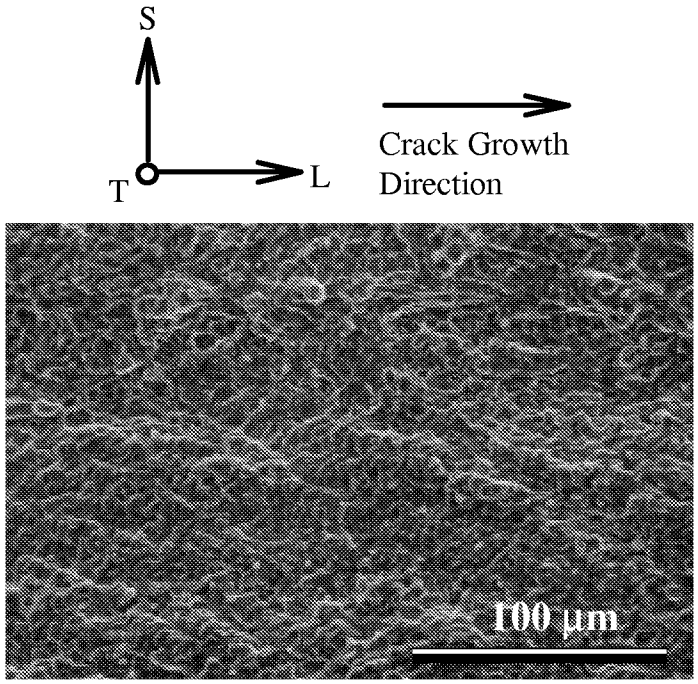

a) room temperature

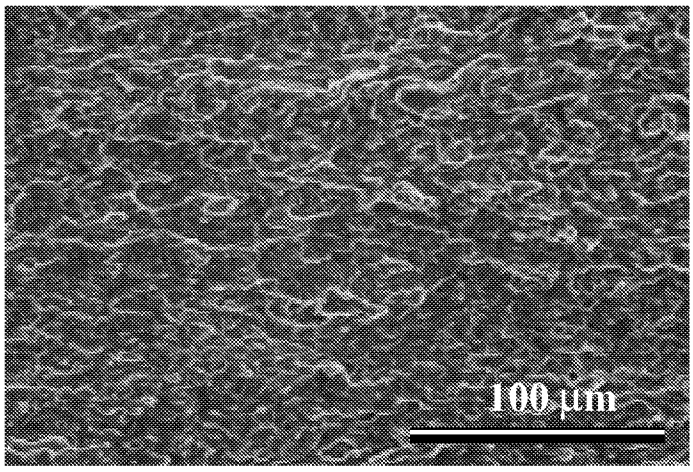

b) 177 °C

Figure 26. SEM micrographs of fatigue surface of Ti 6-2-2-2-2, T-L orientation, $\Delta K = 16.8$ MPa$\sqrt{m}$, $R = 0.5$ tested at a) 24 °C and b) 177 °C in ultrahigh vacuum.

Appendix A – Crack length and stress-intensity factor determinations for the ESE(T) specimen.

A compliance expression to determine crack length (a) for displacements measured along the front-face of an ESE(T) specimen has been derived [28].

$$\frac{a}{W} = C_0 + C_1(U) + C_2(U)^2 + C_3(U)^3 + C_4(U)^4 + C_5(U)^5 \qquad \text{(A-1)}$$

Where $U = \frac{1}{\sqrt{EvB/P} + 1}$, W is the specimen width (Fig. 4), B is the specimen thickness (Fig. 4), P is the applied load, v is the displacement, and E is the elastic modulus. The coefficients for each term have been solved as C_0 = 1.00132, C_1 = -3.58451, C_2 = 6.59954, C_3 = -19.22577, C_4 = 41.54678, C_5 = -31.75871.

A compliance solution for strain measurements along the back-face of an ESE(T) specimen has also been derived [28].

$$\frac{a}{W} = N_0 + N_1(\log A) + N_2(\log A)^2 + N_3(\log A)^3 + N_4(\log A)^4 \qquad \text{(A-2)}$$

Where: $A = (\varepsilon / P)BWE$, and ε is the measured strain. The coefficients for each term have been solved as N_0 = 0.09889, N_1 = 0.41967, N_2 = 0.06751, N_3 = -0.07018, N_4 = 0.01082.

The crack-tip stress-intensity factor expression for the ESE(T) specimens is [28]:

$$K = \left[\frac{P}{B\sqrt{W}}\right] F_{ec} \qquad \text{(A-3)}$$

where:

$$F_{ec} = \frac{(2+\beta)}{(1-\beta)^{3/2}\left(1-\frac{d}{W}\right)^{1/2}} G \qquad \text{(A-4)}$$

$$G = 1.15 + 0.94\beta - 2.48\beta^2 + 2.95\beta^3 - 1.24\beta^4 \qquad \text{(A-5)}$$

$$\beta = \frac{(a-d)}{(W-d)} \qquad \text{(A-6)}$$

and d is the distance between the specimen edge and load line (Fig. 4).

Appendix B - Closure measurements using the compliance techniques.

Load versus strain data was acquired during fatigue testing. The collection of this data during fatigue testing of T-L oriented Ti 6-2-2-2-2 in room temperature laboratory air is identified in Figure 6. From the load versus strain data, strain deviation is calculated as the difference between the measured strains and a least-squares fit through the unloading curve near the maximum load. Load is then normalized by the maximum applied load and plotted against the reduced strain. This technique results in an increased resolution for graphical determination of the crack-opening load. Examples of reduced strain plots are shown in Figures A1, A2, and A3. An opening load is determined on the reduced strain plot when the tangent to the loading curve becomes vertical [11]. The opening load determined from the reduced strain technique is then compared to the opening load values calculated for five selected offset values [7], to determine the appropriate offset level to use for the calculation of ΔK_{op}.

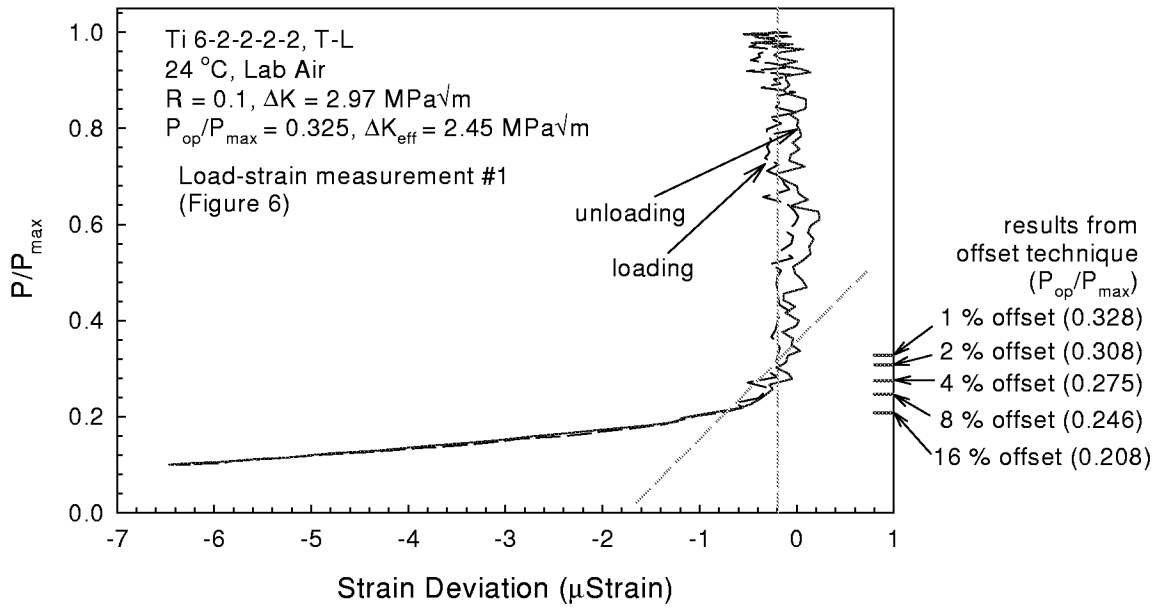

Figure B1. Load versus strain deviation for T-L oriented Ti 6-2-2-2-2 to determine crack opening load. Opening loads determined for 5 different offset values are also shown.

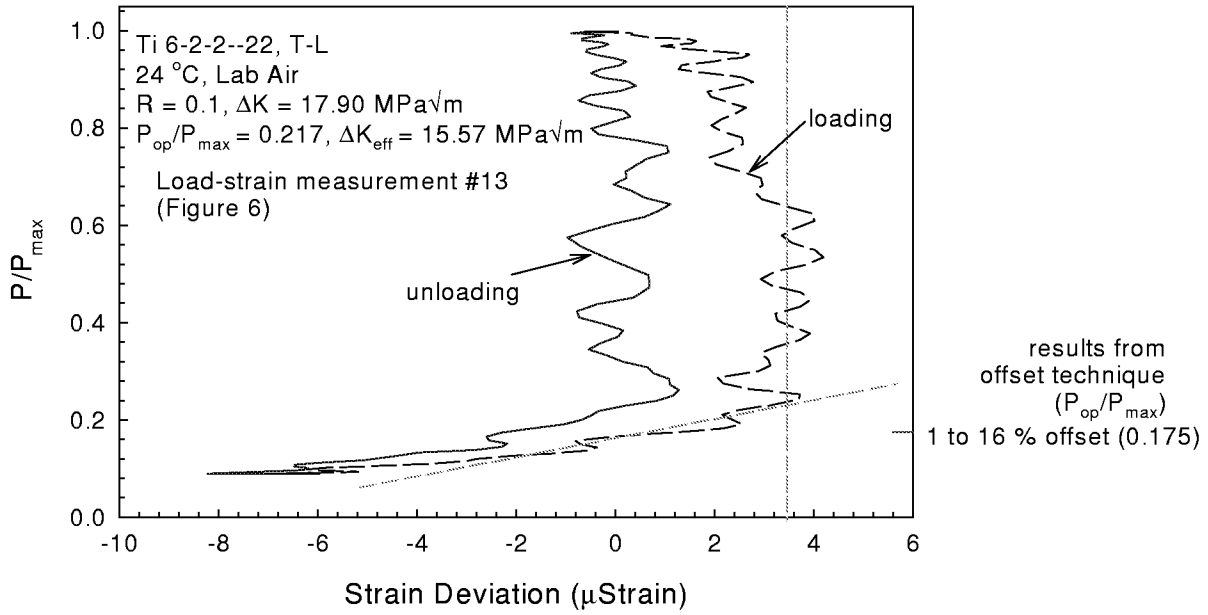

Figure B2. Load versus strain deviation for T-L oriented Ti 6-2-2-2-2 to determine crack-opening load. Opening loads determined for 5 different offset values are also shown.

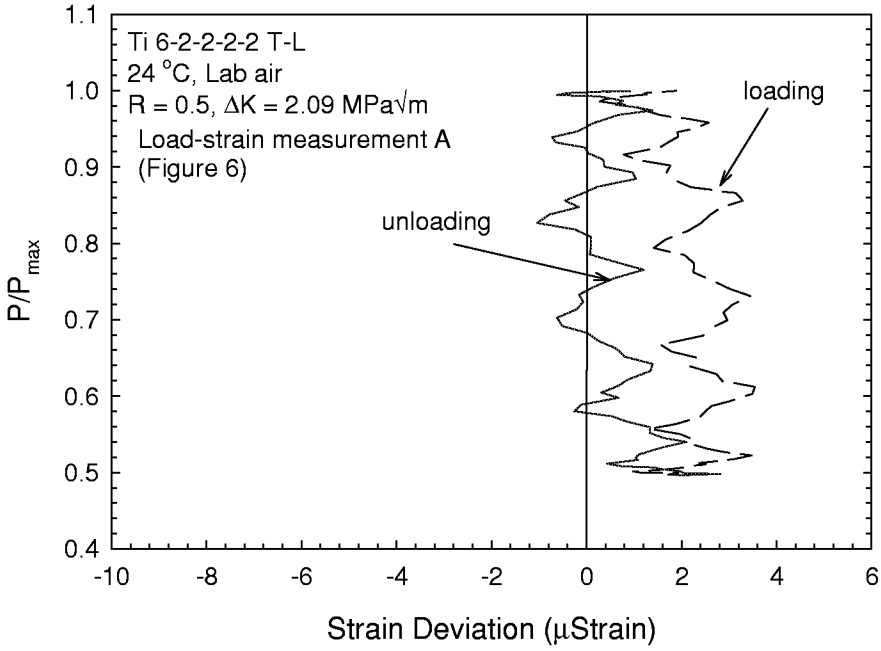

Figure B3. Load versus strain deviation for T-L oriented Ti 6-2-2-2-2 at ΔK = 2.09 MPa√m, R = 0.5 and 5 Hz in room temperature laboratory air. The entire loading portion of the curve is vertical, indicating no crack closure.

Appendix C - Ti 6-2-2-2-2 data in room temperature laboratory air at R = 0.5.

Fatigue crack growth rate (da/dN) and cyclic stress-intensity (ΔK) data for three tests (one K-decreasing and two K-increasing) performed on T-L oriented Ti 6-2-2-2-2 in room temperature laboratory air at R = 0.5 and 5 Hz is listed in Table C1. The tests were conducted in accordance with ASTM E 647 [7] with sinusoidal loading and the normalized K-gradient (C) for each test is listed in Table C1. This data is shown graphically in Figures 5a, 6, 7, 14, 16, and 18. Closure-free ΔK values were determined using the intersection of closure dominated and K_{max} affected results (as demonstrated in Fig. 8).

Table C1: Fatigue crack growth rate data for T-L oriented Ti 6-2-2-2-2 tested in room temperature laboratory air at R = 0.5 and 5 Hz.

da/dN (m/cyl)	ΔK (MPa√m)	closure-free ΔK (MPa√m)	da/dN (m/cyl)	ΔK (MPa√m)	closure-free ΔK (MPa√m)
K-decreasing, C = -0.079 mm^{-1}			1.07E-09	2.54	2.25
2.16E-09	3.07	2.99	1.00E-09	2.52	2.20
2.14E-09	3.05	2.98	9.17E-10	2.51	2.13
2.16E-09	3.04	2.99	9.24E-10	2.49	2.14
2.13E-09	3.02	2.97	9.10E-10	2.48	2.12
2.08E-09	3.00	2.94	9.14E-10	2.46	2.13
2.05E-09	2.98	2.93	9.30E-10	2.45	2.14
1.97E-09	2.96	2.88	8.27E-10	2.43	2.06
1.90E-09	2.95	2.84	7.26E-10	2.42	1.97
1.87E-09	2.93	2.82	7.21E-10	2.40	1.97
1.84E-09	2.91	2.80	7.10E-10	2.39	1.96
1.83E-09	2.89	2.79	7.02E-10	2.37	1.95
1.81E-09	2.88	2.78	6.85E-10	2.36	1.94
1.76E-09	2.86	2.75	6.11E-10	2.35	1.88
1.74E-09	2.84	2.74	5.89E-10	2.33	1.86
1.71E-09	2.82	2.72	6.04E-10	2.32	1.88
1.64E-09	2.81	2.67	5.73E-10	2.30	1.85
1.57E-09	2.79	2.62	5.36E-10	2.29	1.82
1.54E-09	2.77	2.60	5.34E-10	2.28	1.82
1.53E-09	2.76	2.60	5.29E-10	2.26	1.82
1.50E-09	2.74	2.58	4.88E-10	2.25	1.79
1.47E-09	2.72	2.56	4.70E-10	2.24	1.78
1.45E-09	2.71	2.54	4.60E-10	2.22	1.77
1.40E-09	2.69	2.51	4.44E-10	2.21	1.76
1.33E-09	2.68	2.45	4.49E-10	2.20	1.77
1.29E-09	2.66	2.42	4.38E-10	2.18	1.76
1.27E-09	2.64	2.41	3.98E-10	2.17	1.74
1.23E-09	2.63	2.38	3.62E-10	2.16	1.72
1.18E-09	2.61	2.34	3.35E-10	2.15	1.71
1.15E-09	2.60	2.32	3.12E-10	2.13	1.70
1.11E-09	2.58	2.29	2.85E-10	2.12	1.70
1.05E-09	2.57	2.24	2.40E-10	2.11	1.69
1.05E-09	2.55	2.24	8.29E-11	2.09	1.67

Table C1. Continued

da/dN (m/cyl)	ΔK (MPa√m)	closure-free ΔK (MPa√m)	da/dN (m/cyl)	ΔK (MPa√m)	closure-free ΔK (MPa√m)
K-increasing, C=0.16 mm^{-1}			6.98E-09	4.54	
1.39E-09	2.77	2.50	7.53E-09	4.59	
1.42E-09	2.80	2.52	8.09E-09	4.65	
1.46E-09	2.84	2.54	8.24E-09	4.70	
1.55E-09	2.87	2.61	8.54E-09	4.76	
1.61E-09	2.91	2.65	8.95E-09	4.82	
1.61E-09	2.94	2.65	9.22E-09	4.88	
1.73E-09	2.98	2.73	9.59E-09	4.93	
1.94E-09	3.01	2.86	9.97E-09	5.00	
2.05E-09	3.05	2.92	1.02E-08	5.06	
2.11E-09	3.09	2.96	1.05E-08	5.12	
2.15E-09	3.12	2.98	1.10E-08	5.18	
2.27E-09	3.16	3.04	1.17E-08	5.24	
2.37E-09	3.20	3.10	1.21E-08	5.30	
2.39E-09	3.24	3.11	1.23E-08	5.37	
2.43E-09	3.28	3.12	1.29E-08	5.43	
2.55E-09	3.32	3.18	1.39E-08	5.50	
2.73E-09	3.36	3.27	1.45E-08	5.57	
2.83E-09	3.40	3.32	1.50E-08	5.63	
2.91E-09	3.44	3.35	1.57E-08	5.70	
3.06E-09	3.48	3.42	1.64E-08	5.77	
3.24E-09	3.52	3.49	1.71E-08	5.84	
3.37E-09	3.56	3.55	1.80E-08	5.91	
3.50E-09	3.61	3.60	1.87E-08	5.98	
3.69E-09	3.65		1.95E-08	6.06	
3.76E-09	3.70		2.07E-08	6.13	
3.83E-09	3.74		2.17E-08	6.21	
4.01E-09	3.79		2.23E-08	6.28	
4.19E-09	3.83		2.27E-08	6.36	
4.26E-09	3.88		2.34E-08	6.43	
4.34E-09	3.93		2.41E-08	6.51	
4.50E-09	3.97		2.52E-08	6.59	
4.74E-09	4.02		2.60E-08	6.67	
4.96E-09	4.07		2.68E-08	6.75	
5.19E-09	4.12		2.80E-08	6.83	
5.39E-09	4.17		2.88E-08	6.91	
5.56E-09	4.22		2.99E-08	7.00	
5.73E-09	4.27		3.13E-08	7.09	
5.98E-09	4.32		3.26E-08	7.17	
6.15E-09	4.37		3.46E-08	7.26	
6.28E-09	4.43		3.62E-08	7.35	
6.62E-09	4.48		3.67E-08	7.44	

Table C1. Continued

da/dN (m/cyl)	ΔK (MPa√m)	da/dN (m/cyl)	ΔK (MPa√m)	da/dN (m/cyl)	ΔK (MPa√m)
K-inc., C=0.16 mm^{-1} (cont.)		1.41E-07	12.33	K-inc., C=0.16 mm^{-1}	
3.78E-08	7.52	1.45E-07	12.48	9.29E-09	5.04
3.98E-08	7.62	1.45E-07	12.63	9.76E-09	5.10
4.21E-08	7.71	1.47E-07	12.78	1.03E-08	5.16
4.46E-08	7.80	1.51E-07	12.94	1.08E-08	5.23
4.72E-08	7.90	1.53E-07	13.10	1.12E-08	5.29
4.81E-08	7.99	1.57E-07	13.26	1.14E-08	5.36
4.81E-08	8.09	1.62E-07	13.41	1.17E-08	5.42
4.99E-08	8.19	1.64E-07	13.58	1.27E-08	5.57
5.20E-08	8.28	1.67E-07	13.74	1.28E-08	5.62
5.30E-08	8.38	1.74E-07	13.91	1.35E-08	5.69
5.28E-08	8.48	1.81E-07	14.08	1.43E-08	5.76
5.31E-08	8.59	1.85E-07	14.26	1.51E-08	5.83
5.61E-08	8.69	1.88E-07	14.43	1.57E-08	5.91
5.81E-08	8.80	1.93E-07	14.60	1.61E-08	5.97
5.88E-08	8.91	1.80E-07	14.77	1.67E-08	6.05
6.18E-08	9.02	2.06E-07	15.15	1.73E-08	6.12
6.54E-08	9.12	2.23E-07	15.25	1.81E-08	6.19
6.81E-08	9.24	2.34E-07	15.57	1.89E-08	6.27
7.03E-08	9.34	2.27E-07	15.63	2.00E-08	6.35
7.24E-08	9.46	2.27E-07	15.74	2.12E-08	6.42
7.40E-08	9.57	2.33E-07	15.89	2.18E-08	6.50
7.46E-08	9.69	2.36E-07	16.08	2.27E-08	6.58
7.52E-08	9.81	2.41E-07	16.28	2.37E-08	6.66
7.81E-08	9.93	2.48E-07	16.47	2.43E-08	6.73
8.21E-08	10.05	2.56E-07	16.67	2.52E-08	6.82
8.48E-08	10.17	2.60E-07	16.87	2.63E-08	6.90
8.71E-08	10.29	2.63E-07	17.08	2.73E-08	6.99
9.06E-08	10.42	2.76E-07	17.28	2.69E-08	7.07
9.48E-08	10.55	2.98E-07	17.49	2.93E-08	7.21
9.76E-08	10.67	3.21E-07	17.70	3.07E-08	7.28
1.01E-07	10.80	3.50E-07	17.92	3.18E-08	7.37
1.06E-07	10.93	3.69E-07	18.13	3.29E-08	7.46
1.10E-07	11.06	3.82E-07	18.37	3.41E-08	7.55
1.13E-07	11.20	3.87E-07	18.58	3.56E-08	7.65
1.16E-07	11.33	3.90E-07	18.81	3.70E-08	7.73
1.17E-07	11.47	3.82E-07	19.04	3.83E-08	7.82
1.18E-07	11.61	4.08E-07	19.32	4.05E-08	7.92
1.22E-07	11.75			4.25E-08	8.02
1.26E-07	11.90			4.44E-08	8.12
1.29E-07	12.04			4.64E-08	8.22
1.34E-07	12.19			4.85E-08	8.32

Table C1. Continued

da/dN (m/cyl)	ΔK (MPa√m)	da/dN (m/cyl)	ΔK (MPa√m)	da/dN (m/cyl)	ΔK (MPa√m)
K-inc., C=0.16 mm^{-1} (cont.)		2.00E-07	14.62	9.28E-07	24.44
5.03E-08	8.42	2.05E-07	14.80	1.18E-06	24.77
5.20E-08	8.51	2.10E-07	14.98	1.44E-06	25.03
5.39E-08	8.61	2.16E-07	15.16	1.96E-06	25.41
5.72E-08	8.99	2.22E-07	15.35	2.47E-06	25.65
5.95E-08	9.10	2.29E-07	15.52	3.30E-06	26.03
6.25E-08	9.21	2.36E-07	15.71	4.47E-06	26.35
6.53E-08	9.32	2.46E-07	15.91		
6.72E-08	9.43	2.61E-07	16.09		
6.88E-08	9.55	2.72E-07	16.29		
7.06E-08	9.66	2.71E-07	16.49		
7.18E-08	9.77	2.70E-07	16.69		
7.32E-08	9.89	2.77E-07	16.89		
7.64E-08	10.01	2.89E-07	17.09		
7.93E-08	10.13	3.05E-07	17.29		
8.26E-08	10.26	3.21E-07	17.50		
8.62E-08	10.38	3.29E-07	17.71		
8.88E-08	10.51	3.49E-07	17.93		
9.25E-08	10.64	3.99E-07	18.15		
9.54E-08	10.76	4.27E-07	18.37		
9.87E-08	10.89	4.11E-07	18.59		
1.02E-07	11.02	3.88E-07	18.81		
1.05E-07	11.15	3.92E-07	19.05		
1.10E-07	11.30	4.14E-07	19.26		
1.12E-07	11.43	5.59E-07	19.80		
1.13E-07	11.56	6.63E-07	19.95		
1.17E-07	11.70	6.01E-07	20.17		
1.21E-07	11.85	6.20E-07	20.42		
1.22E-07	11.99	6.20E-07	20.66		
1.24E-07	12.13	6.23E-07	20.91		
1.29E-07	12.28	6.62E-07	21.16		
1.32E-07	12.42	7.19E-07	21.42		
1.35E-07	12.57	7.53E-07	21.68		
1.39E-07	12.73	7.40E-07	21.93		
1.44E-07	12.88	7.28E-07	22.21		
1.78E-07	13.43	7.55E-07	22.47		
1.71E-07	13.60	7.42E-07	22.75		
1.73E-07	13.76	7.24E-07	23.02		
1.76E-07	13.93	7.73E-07	23.30		
1.80E-07	14.10	8.15E-07	23.61		
1.87E-07	14.27	8.05E-07	23.86		
1.95E-07	14.44	8.29E-07	24.19		

Appendix D - Ti 6-2-2-2-2 data in room temperature laboratory air at R = 0.1.

Fatigue crack growth rate (da/dN), cyclic stress-intensity (ΔK) and effective cyclic stress-intensity (ΔK_{eff}) data for two tests (one K-decreasing and one K-increasing) performed on T-L oriented Ti 6-2-2-2-2 in room temperature laboratory air at R = 0.1 and 5 Hz is listed in Table D1. The tests were conducted in accordance with ASTM E 647 [7] with sinusoidal loading and the normalized K-gradient (C) for each test is listed in Table D1. This data is shown graphically in Figures 6, 7, and 13. Closure-free ΔK values, determined using the intersection of closure dominated and K_{max} affected results (as demonstrated in Fig. 8), for da/dN less than 1 x 10^{-7} m/cycle are also presented.

Table D1: Fatigue crack growth rate data for T-L oriented Ti 6-2-2-2-2 tested in room temperature laboratory air at R = 0.1 and 5 Hz.

da/dN (m/cyl)	ΔK (MPa$\sqrt{m}$)	closure-free ΔK (MPa$\sqrt{m}$)	da/dN (m/cyl)	ΔK (MPa$\sqrt{m}$)	closure-free ΔK (MPa$\sqrt{m}$)
K-decreasing, C = -0.079 mm^{-1}			1.22E-09	3.59	2.39
3.02E-09	4.34	3.47	1.18E-09	3.56	2.36
2.80E-09	4.30	3.37	1.17E-09	3.54	2.35
2.77E-09	4.28	3.35	1.11E-09	3.52	2.30
2.83E-09	4.25	3.39	1.10E-09	3.50	2.30
2.78E-09	4.23	3.36	1.07E-09	3.48	2.27
2.60E-09	4.20	3.27	1.04E-09	3.46	2.25
2.56E-09	4.18	3.25	1.04E-09	3.44	2.25
2.53E-09	4.15	3.23	9.72E-10	3.42	2.19
2.53E-09	4.12	3.24	9.12E-10	3.39	2.14
2.49E-09	4.10	3.21	8.96E-10	3.37	2.13
2.30E-09	4.08	3.11	8.63E-10	3.35	2.10
2.25E-09	4.05	3.08	8.17E-10	3.33	2.06
2.10E-09	4.03	2.99	7.84E-10	3.31	2.03
2.01E-09	4.00	2.94	7.59E-10	3.29	2.01
2.14E-09	3.98	3.02	7.04E-10	3.27	1.97
2.12E-09	3.95	3.01	6.99E-10	3.25	1.96
2.10E-09	3.93	3.00	7.00E-10	3.23	1.96
2.03E-09	3.91	2.95	6.61E-10	3.21	1.93
1.92E-09	3.88	2.88	6.32E-10	3.20	1.91
1.83E-09	3.86	2.83	6.15E-10	3.18	1.89
1.71E-09	3.83	2.75	6.04E-10	3.16	1.89
1.64E-09	3.81	2.70	5.53E-10	3.14	1.85
1.59E-09	3.79	2.66	5.20E-10	3.12	1.82
1.53E-09	3.77	2.62	5.04E-10	3.10	1.81
1.50E-09	3.74	2.60	4.61E-10	3.08	1.78
1.50E-09	3.72	2.60	4.51E-10	3.06	1.78
1.48E-09	3.70	2.59	4.42E-10	3.04	1.77
1.49E-09	3.67	2.59	3.94E-10	3.03	1.75
1.44E-09	3.65	2.56	3.32E-10	3.01	1.72
1.34E-09	3.63	2.48	2.95E-10	2.99	1.71
1.29E-09	3.61	2.45	2.72E-10	2.97	1.71
1.29E-09	3.61	2.45	3.43E-11	2.95	1.69

Table D1. Continued

da/dN (m/cyl)	ΔK (MPa√m)	closure-free ΔK (MPa√m)	da/dN (m/cyl)	ΔK (MPa√m)	closure-free ΔK (MPa√m)
K-increasing, C=0.16 mm^{-1}			1.07E-08	6.54	5.36
2.17E-09	4.00	3.04	1.16E-08	6.61	5.50
2.14E-09	4.04	3.02	1.21E-08	6.70	5.57
2.21E-09	4.09	3.06	1.20E-08	6.77	5.55
2.33E-09	4.14	3.12	1.26E-08	6.86	5.63
2.49E-09	4.19	3.21	1.38E-08	6.94	5.79
2.52E-09	4.24	3.23	1.34E-08	7.02	5.73
2.52E-09	4.29	3.22	1.41E-08	7.11	5.82
2.61E-09	4.34	3.27	1.49E-08	7.20	5.92
2.71E-09	4.40	3.32	1.52E-08	7.28	5.95
2.90E-09	4.45	3.41	1.63E-08	7.37	6.08
3.08E-09	4.51	3.50	1.71E-08	7.46	6.17
3.17E-09	4.56	3.53	1.73E-08	7.55	6.18
3.25E-09	4.62	3.57	1.89E-08	7.64	6.36
3.27E-09	4.67	3.57	2.00E-08	7.73	6.47
3.41E-09	4.73	3.63	2.06E-08	7.83	6.53
3.64E-09	4.78	3.73	2.21E-08	7.92	6.67
3.77E-09	4.84	3.78	2.18E-08	8.01	6.64
3.85E-09	4.90	3.80	2.27E-08	8.11	6.72
3.99E-09	4.96	3.85	2.45E-08	8.21	6.89
4.16E-09	5.02	3.91	2.62E-08	8.31	7.04
4.34E-09	5.08	3.98	2.61E-08	8.41	7.02
4.49E-09	5.14	4.02	2.72E-08	8.52	7.11
4.71E-09	5.21	4.09	2.98E-08	8.61	7.33
5.02E-09	5.27	4.19	2.98E-08	8.72	7.32
5.27E-09	5.33	4.26	3.08E-08	8.82	7.40
5.54E-09	5.40	4.34	3.30E-08	8.93	7.58
5.65E-09	5.46	4.37	3.42E-08	9.04	7.66
5.67E-09	5.52	4.37	3.50E-08	9.15	7.72
6.03E-09	5.59	4.46	3.84E-08	9.26	7.98
6.44E-09	5.66	4.56	4.03E-08	9.37	8.11
6.44E-09	5.73	4.56	3.89E-08	9.48	8.00
6.64E-09	5.80	4.60	4.12E-08	9.60	8.16
6.88E-09	5.87	4.66	4.27E-08	9.71	8.26
7.46E-09	5.94	4.79	4.44E-08	9.82	8.38
7.74E-09	6.00	4.84	4.83E-08	9.94	8.64
7.91E-09	6.08	4.87	5.02E-08	10.06	8.76
8.48E-09	6.15	4.99	5.37E-08	10.18	8.99
8.96E-09	6.23	5.07	5.63E-08	10.31	9.15
9.51E-09	6.31	5.17	5.74E-08	10.44	9.21
9.94E-09	6.38	5.24	5.71E-08	10.56	9.18
1.01E-08	6.46	5.26	5.89E-08	10.70	9.28

Table D1. Continued

da/dN (m/cyl)	ΔK (MPa√m)	closure-free ΔK (MPa√m)	da/dN (m/cyl)	ΔK (MPa√m)	closure-free ΔK (MPa√m)
K-increasing, C=0.16 mm^{-1} (cont.)			2.04E-07	17.69	
6.02E-08	10.82	9.36	2.15E-07	17.89	
6.10E-08	10.95	9.40	2.16E-07	18.11	
6.42E-08	11.08	9.59	2.17E-07	18.33	
6.57E-08	11.21	9.67	2.18E-07	18.55	
6.78E-08	11.35	9.78	2.39E-07	18.79	
7.09E-08	11.49	9.95	2.50E-07	19.00	
7.27E-08	11.63	10.05	2.34E-07	19.24	
7.70E-08	11.77	10.28	2.35E-07	19.46	
8.11E-08	11.91	10.50	2.49E-07	19.70	
8.25E-08	12.05	10.57	2.51E-07	19.93	
8.71E-08	12.20	10.80	2.65E-07	20.18	
8.95E-08	12.34	10.92	2.62E-07	20.42	
9.51E-08	12.49	11.19	2.57E-07	20.69	
9.44E-08	12.64	11.15	2.79E-07	20.91	
9.82E-08	12.80	11.32	2.84E-07	21.19	
1.05E-07	12.95		2.93E-07	21.43	
1.03E-07	13.11		2.86E-07	21.68	
1.02E-07	13.26		3.00E-07	21.97	
1.04E-07	13.42		3.09E-07	22.20	
1.13E-07	13.59		3.07E-07	22.49	
1.13E-07	13.75		3.33E-07	22.76	
1.14E-07	13.92		3.38E-07	23.02	
1.26E-07	14.08		3.41E-07	23.32	
1.32E-07	14.26		3.43E-07	23.58	
1.34E-07	14.43		3.64E-07	23.88	
1.38E-07	14.60		3.79E-07	24.15	
1.42E-07	14.78		3.78E-07	24.45	
1.47E-07	14.96		4.00E-07	24.73	
1.54E-07	15.15		4.07E-07	25.04	
1.56E-07	15.33		4.08E-07	25.33	
1.59E-07	15.51		4.28E-07	25.68	
1.65E-07	15.69		4.49E-07	25.93	
1.71E-07	15.88		5.57E-07	26.33	
1.80E-07	16.07		5.56E-07	26.57	
1.77E-07	16.27		5.03E-07	26.94	
1.74E-07	16.46		5.07E-07	27.23	
1.84E-07	16.66		5.07E-07	27.59	
1.91E-07	16.86		5.09E-07	27.88	
1.96E-07	17.08		5.27E-07	28.24	
2.01E-07	17.28		6.05E-07	28.57	
1.97E-07	17.49		6.30E-07	28.90	

Table D1. Continued

da/dN (m/cyl)	ΔK (MPa√m)	closure-free ΔK (MPa√m)	da/dN (m/cyl)	ΔK (MPa√m)	closure-free ΔK (MPa√m)
K-increasing, C=0.16 mm^{-1} (cont.)			2.04E-06	35.89	
6.49E-07	29.25		2.25E-06	36.31	
7.16E-07	29.60		2.60E-06	36.76	
7.51E-07	29.97		2.74E-06	37.18	
8.02E-07	30.35		2.98E-06	37.69	
8.78E-07	30.73		3.12E-06	38.10	
9.49E-07	31.12		2.95E-06	38.59	
9.29E-07	31.45		3.26E-06	39.11	
9.50E-07	31.85		3.36E-06	39.52	
1.00E-06	32.20		3.44E-06	40.08	
1.09E-06	32.63		4.09E-06	40.51	
1.24E-06	33.00		4.60E-06	40.99	
1.37E-06	33.43		5.09E-06	41.47	
1.41E-06	33.79		5.31E-06	41.97	
1.52E-06	34.22		5.45E-06	42.48	
1.64E-06	34.60		6.20E-06	43.00	
1.71E-06	35.05		7.41E-06	43.58	
1.89E-06	35.46		7.72E-06	44.04	

Appendix E - Ti 6-2-2-2-2 data in 177°C laboratory air at R = 0.5.

Fatigue crack growth rate (da/dN) and cyclic stress-intensity (ΔK) data for three tests (one K-decreasing and two K-increasing) performed on T-L oriented Ti 6-2-2-2-2 in 177 °C laboratory air at R = 0.5 and 5 Hz is listed in Table E1. The tests were conducted in accordance with ASTM E 647 [7] with sinusoidal loading and the normalized K-gradient (C) for each test is listed in Table E1. This data is shown graphically in Figures 10, 11 and 14. Closure-free ΔK values, determined using the intersection of closure dominated and K_{max} affected results (as demonstrated in Fig. 8), are also presented.

Table E1: Fatigue crack growth rate data for T-L oriented Ti 6-2-2-2-2 tested in 177 °C laboratory air at R = 0.5 and 5 Hz.

da/dN (m/cyl)	ΔK (MPa√m)	closure-free ΔK (MPa√m)	da/dN (m/cyl)	ΔK (MPa√m)	closure-free ΔK (MPa√m)
K-decreasing, C = -0.079 mm^{-1}			2.58E-09	3.48	3.27
4.81E-09	4.22	4.16	2.53E-09	3.46	3.24
4.61E-09	4.19	4.09	2.47E-09	3.44	3.21
4.52E-09	4.17	4.06	2.40E-09	3.42	3.18
4.36E-09	4.14	4.01	2.35E-09	3.40	3.15
4.18E-09	4.12	3.94	2.33E-09	3.38	3.14
4.05E-09	4.09	3.89	2.32E-09	3.36	3.13
4.00E-09	4.07	3.88	2.28E-09	3.34	3.11
3.95E-09	4.05	3.86	2.24E-09	3.32	3.09
3.93E-09	4.02	3.85	2.20E-09	3.30	3.07
3.92E-09	4.00	3.85	2.16E-09	3.28	3.05
3.80E-09	3.97	3.80	2.16E-09	3.26	3.05
3.60E-09	3.95	3.72	2.12E-09	3.24	3.03
3.53E-09	3.93	3.69	2.08E-09	3.22	3.00
3.51E-09	3.90	3.68	2.09E-09	3.20	3.01
3.45E-09	3.88	3.66	2.09E-09	3.18	3.01
3.42E-09	3.86	3.65	2.05E-09	3.16	2.99
3.34E-09	3.83	3.61	1.99E-09	3.14	2.95
3.30E-09	3.81	3.60	1.93E-09	3.13	2.92
3.28E-09	3.79	3.59	1.90E-09	3.11	2.90
3.21E-09	3.76	3.56	1.92E-09	3.09	2.91
3.10E-09	3.74	3.51	1.91E-09	3.07	2.91
3.04E-09	3.72	3.48	1.84E-09	3.05	2.86
3.05E-09	3.70	3.49	1.72E-09	3.01	2.79
2.98E-09	3.67	3.46	1.72E-09	2.99	2.79
2.88E-09	3.65	3.41	1.70E-09	2.98	2.78
2.92E-09	3.63	3.43	1.68E-09	2.96	2.77
2.88E-09	3.61	3.41	1.66E-09	2.94	2.75
2.77E-09	3.59	3.36	1.62E-09	2.92	2.73
2.71E-09	3.57	3.33	1.60E-09	2.90	2.72
2.70E-09	3.54	3.33	1.58E-09	2.89	2.70
2.67E-09	3.52	3.31	1.53E-09	2.87	2.67
2.61E-09	3.50	3.28	1.54E-09	2.85	2.68

Table E1. Continued

da/dN (m/cyl)	ΔK (MPa√m)	closure-free ΔK (MPa√m)	da/dN (m/cyl)	ΔK (MPa√m)	closure-free ΔK (MPa√m)
K-decreasing, C=-0.079 mm^{-1} (cont.)			1.06E-10	2.22	1.95
1.55E-09	2.84	2.68			
1.50E-09	2.82	2.65			
1.45E-09	2.80	2.62	K-increasing, C = 0.16 mm^{-1}		
1.43E-09	2.78	2.60	3.29E-09	3.72	3.60
1.42E-09	2.77	2.60	3.38E-09	3.77	3.63
1.38E-09	2.75	2.57	3.56E-09	3.82	3.71
1.32E-09	2.74	2.53	3.66E-09	3.87	3.75
1.28E-09	2.72	2.50	3.76E-09	3.91	3.79
1.24E-09	2.70	2.48	3.92E-09	3.96	3.85
1.16E-09	2.69	2.42	4.11E-09	4.01	3.92
1.12E-09	2.67	2.39	4.29E-09	4.06	3.98
1.11E-09	2.65	2.38	4.36E-09	4.11	4.01
1.10E-09	2.64	2.38	4.46E-09	4.16	4.04
1.10E-09	2.62	2.38	4.57E-09	4.21	4.08
1.07E-09	2.61	2.36	4.62E-09	4.26	4.09
1.01E-09	2.59	2.31	4.77E-09	4.31	4.14
9.62E-10	2.58	2.28	5.02E-09	4.36	4.22
9.51E-10	2.56	2.27	5.16E-09	4.42	4.27
9.72E-10	2.55	2.29	5.17E-09	4.47	4.27
9.64E-10	2.53	2.28	5.39E-09	4.52	4.33
9.10E-10	2.52	2.24	5.70E-09	4.58	4.43
8.77E-10	2.50	2.22	5.88E-09	4.63	4.48
8.67E-10	2.49	2.21	5.96E-09	4.69	4.50
8.53E-10	2.47	2.20	6.07E-09	4.75	4.53
8.15E-10	2.46	2.18	6.35E-09	4.80	4.60
7.66E-10	2.44	2.14	6.72E-09	4.86	4.70
7.34E-10	2.43	2.12	7.07E-09	4.92	4.79
6.94E-10	2.41	2.10	7.26E-09	4.98	4.83
6.59E-10	2.40	2.07	7.45E-09	5.04	4.88
6.52E-10	2.38	2.07	7.77E-09	5.10	4.95
6.32E-10	2.37	2.06	8.07E-09	5.16	5.02
5.99E-10	2.35	2.04	8.36E-09	5.23	5.08
5.57E-10	2.34	2.01	8.55E-09	5.29	5.12
5.12E-10	2.33	1.99	8.80E-09	5.35	5.17
4.71E-10	2.31	1.97	9.32E-09	5.42	5.28
4.48E-10	2.30	1.96	9.65E-09	5.48	5.34
4.10E-10	2.29	1.95	1.00E-08	5.55	5.41
3.27E-10	2.27	1.94	1.05E-08	5.62	5.50
3.06E-10	2.26	1.94	1.07E-08	5.69	5.54
2.83E-10	2.24	1.94	1.11E-08	5.76	5.61
2.05E-10	2.23	1.96	1.14E-08	5.82	5.66

Table E1. Continued

da/dN (m/cyl)	ΔK (MPa√m)	closure-free ΔK (MPa√m)	da/dN (m/cyl)	ΔK (MPa√m)	closure-free ΔK (MPa√m)
K-increasing, C=0.16 mm^{-1} (cont.)			4.82E-08	9.65	
1.19E-08	5.89	5.75	4.94E-08	9.77	
1.25E-08	5.96	5.85	5.10E-08	9.88	
1.28E-08	6.04	5.90	5.24E-08	10.00	
1.32E-08	6.11	5.96	5.39E-08	10.12	
1.37E-08	6.18	6.04	5.58E-08	10.24	
1.40E-08	6.26	6.08	5.83E-08	10.37	
1.44E-08	6.33	6.14	5.97E-08	10.50	
1.51E-08	6.41		6.03E-08	10.62	
1.59E-08	6.49		6.13E-08	10.75	
1.67E-08	6.57		9.50E-08	13.14	
1.75E-08	6.65		9.65E-08	13.14	
1.82E-08	6.73		9.63E-08	13.14	
1.87E-08	6.81		9.67E-08	13.14	
1.92E-08	6.89		9.81E-08	13.14	
2.00E-08	6.97		9.71E-08	13.14	
2.07E-08	7.06		9.58E-08	13.14	
2.12E-08	7.14		2.16E-07	19.72	
2.22E-08	7.23		2.15E-07	19.72	
2.33E-08	7.32		2.14E-07	19.72	
2.42E-08	7.41		2.19E-07	19.72	
2.51E-08	7.50		2.24E-07	19.72	
2.59E-08	7.59		2.23E-07	19.72	
2.64E-08	7.68		2.23E-07	20.06	
2.75E-08	7.77		2.25E-07	20.32	
2.89E-08	7.86		2.31E-07	20.56	
3.01E-08	7.96		2.36E-07	20.82	
3.16E-08	8.06		2.39E-07	21.07	
3.28E-08	8.15		2.43E-07	21.33	
3.42E-08	8.25		2.47E-07	21.58	
3.47E-08	8.35		2.51E-07	21.84	
3.50E-08	8.45		2.57E-07	22.10	
3.57E-08	8.56		2.58E-07	22.36	
3.68E-08	8.66		2.63E-07	22.63	
3.75E-08	8.76		2.67E-07	22.91	
3.86E-08	8.87		2.76E-07	23.20	
4.03E-08	8.98		2.82E-07	23.47	
4.15E-08	9.08		2.84E-07	23.76	
4.29E-08	9.19		2.85E-07	24.04	
4.39E-08	9.30		3.02E-07	24.34	
4.48E-08	9.42		3.27E-07	24.63	
4.66E-08	9.53		3.53E-07	24.94	

Table E1. Continued

da/dN (m/cyl)	ΔK (MPa√m)	da/dN (m/cyl)	ΔK (MPa√m)	da/dN (m/cyl)	ΔK (MPa√m)
K-inc., C=0.16 mm^{-1} (cont.)		1.81E-08	6.66	3.64E-08	8.81
3.98E-07	25.24	1.85E-08	6.70	3.67E-08	8.87
4.10E-07	25.53	1.88E-08	6.76	3.72E-08	8.92
3.96E-07	25.84	1.90E-08	6.81	3.80E-08	8.98
3.89E-07	26.15	1.95E-08	6.85	3.88E-08	9.04
3.84E-07	26.46	1.99E-08	6.90	3.95E-08	9.10
3.90E-07	26.80	2.04E-08	6.94	4.04E-08	9.15
4.05E-07	27.13	2.07E-08	6.99	4.12E-08	9.21
4.17E-07	27.46	2.06E-08	7.03	4.19E-08	9.27
4.31E-07	27.79	2.12E-08	7.10	4.26E-08	9.33
4.52E-07	28.11	2.18E-08	7.15	4.28E-08	9.39
4.77E-07	28.46	2.23E-08	7.22	4.25E-08	9.45
4.83E-07	28.80	2.28E-08	7.26	4.28E-08	9.51
4.80E-07	29.15	2.33E-08	7.31	4.39E-08	9.57
5.21E-07	29.49	2.35E-08	7.36	4.48E-08	9.64
6.06E-07	29.84	2.39E-08	7.41	4.55E-08	9.70
6.48E-07	30.21	2.43E-08	7.45	4.64E-08	9.76
6.25E-07	30.58	2.43E-08	7.50	4.71E-08	9.82
6.25E-07	30.98	2.48E-08	7.55	4.77E-08	9.88
6.74E-07	31.36	2.57E-08	7.60	4.83E-08	9.95
7.29E-07	31.75	2.59E-08	7.65	4.94E-08	10.01
7.74E-07	32.13	2.61E-08	7.70	5.07E-08	10.08
8.30E-07	32.50	2.66E-08	7.75	5.14E-08	10.14
9.27E-07	32.87	2.69E-08	7.80	5.16E-08	10.21
		2.74E-08	7.85	5.22E-08	10.27
		2.82E-08	7.90	5.30E-08	10.34
K-inc., C = 0.16 mm^{-1}		2.86E-08	7.95	5.37E-08	10.40
1.34E-08	5.96	2.93E-08	8.00	5.46E-08	10.47
1.37E-08	6.00	2.97E-08	8.05	5.50E-08	10.54
1.38E-08	6.06	2.98E-08	8.10	5.53E-08	10.61
1.39E-08	6.10	3.03E-08	8.16	5.64E-08	10.67
1.42E-08	6.14	3.09E-08	8.21	5.70E-08	10.74
1.44E-08	6.18	3.12E-08	8.26	5.84E-08	10.84
1.47E-08	6.22	3.16E-08	8.32	5.95E-08	10.91
1.52E-08	6.28	3.21E-08	8.37	6.11E-08	11.02
1.55E-08	6.32	3.23E-08	8.42	6.14E-08	11.09
1.59E-08	6.38	3.28E-08	8.48	6.18E-08	11.16
1.62E-08	6.42	3.34E-08	8.53	6.33E-08	11.23
1.65E-08	6.46	3.39E-08	8.59	6.39E-08	11.31
1.69E-08	6.51	3.44E-08	8.64	6.42E-08	11.38
1.72E-08	6.55	3.54E-08	8.70	6.62E-08	11.45
1.75E-08	6.59	3.60E-08	8.75	6.75E-08	11.52

Table E1. Continued

da/dN (m/cyl)	ΔK (MPa√m)	da/dN (m/cyl)	ΔK (MPa√m)	da/dN (m/cyl)	ΔK (MPa√m)
K-inc., C=0.16 mm^{-1}(cont.)		1.22E-07	15.46	2.05E-07	20.54
6.80E-08	11.60	1.24E-07	15.56	2.08E-07	20.67
6.97E-08	11.71	1.24E-07	15.66	2.12E-07	20.87
7.04E-08	11.78	1.26E-07	15.76	2.14E-07	21.01
7.11E-08	11.90	1.27E-07	15.86	2.17E-07	21.14
7.24E-08	11.98	1.30E-07	15.96	2.21E-07	21.28
7.31E-08	12.05	1.30E-07	16.06	2.23E-07	21.41
7.32E-08	12.13	1.32E-07	16.16	2.22E-07	21.55
7.37E-08	12.21	1.35E-07	16.27	2.21E-07	21.69
7.45E-08	12.28	1.36E-07	16.37	2.24E-07	21.83
7.57E-08	12.36	1.40E-07	16.48	2.28E-07	21.97
7.68E-08	12.44	1.42E-07	16.58	2.29E-07	22.11
7.84E-08	12.52	1.44E-07	16.69	2.29E-07	22.25
7.97E-08	12.60	1.45E-07	16.80	2.30E-07	22.49
8.01E-08	12.68	1.48E-07	16.91	2.34E-07	22.68
8.10E-08	12.80	1.50E-07	17.01	2.41E-07	22.93
8.21E-08	12.89	1.50E-07	17.12	2.45E-07	23.12
8.42E-08	13.01	1.51E-07	17.23	2.47E-07	23.27
8.54E-08	13.09	1.54E-07	17.34	2.48E-07	23.42
8.63E-08	13.18	1.57E-07	17.45	2.51E-07	23.57
8.68E-08	13.26	1.57E-07	17.57	2.54E-07	23.72
8.83E-08	13.35	1.56E-07	17.68	2.55E-07	23.87
9.03E-08	13.43	1.60E-07	17.85	2.60E-07	24.02
9.12E-08	13.52	1.62E-07	17.96	2.62E-07	24.18
9.22E-08	13.60	1.65E-07	18.14	2.61E-07	24.33
9.38E-08	13.69	1.70E-07	18.25	2.63E-07	24.49
9.51E-08	13.78	1.72E-07	18.37	2.64E-07	24.65
9.58E-08	13.87	1.73E-07	18.49	2.70E-07	24.80
9.68E-08	14.00	1.75E-07	18.61	2.70E-07	24.97
9.83E-08	14.09	1.76E-07	18.73	2.68E-07	25.13
1.01E-07	14.23	1.77E-07	18.85	2.69E-07	25.29
1.02E-07	14.32	1.79E-07	18.97	2.76E-07	25.46
1.04E-07	14.41	1.81E-07	19.09	2.83E-07	25.61
1.05E-07	14.50	1.86E-07	19.27	2.90E-07	25.78
1.07E-07	14.59	1.89E-07	19.39	2.96E-07	25.94
1.08E-07	14.69	1.88E-07	19.58	2.70E-07	26.58
1.10E-07	14.78	1.91E-07	19.71	2.77E-07	26.70
1.12E-07	14.92	1.92E-07	19.82	2.95E-07	26.96
1.12E-07	15.02	1.93E-07	19.96	3.01E-07	27.13
1.14E-07	15.16	1.95E-07	20.08	3.08E-07	27.31
1.18E-07	15.26	1.97E-07	20.22	3.20E-07	27.48
1.20E-07	15.36	2.00E-07	20.35	3.25E-07	27.65

Table E1. Continued

da/dN (m/cyl)	ΔK (MPa√m)	da/dN (m/cyl)	ΔK (MPa√m)	da/dN (m/cyl)	ΔK (MPa√m)
K-inc., C=0.16 mm^{-1}(cont.)		5.54E-07	32.59	1.16E-06	37.85
3.29E-07	27.83	5.79E-07	32.89	1.19E-06	38.10
3.76E-07	28.02	5.75E-07	33.11	1.20E-06	38.33
3.77E-07	28.19	5.91E-07	33.32	1.20E-06	38.59
3.37E-07	28.38	6.35E-07	33.53	1.20E-06	38.82
3.49E-07	28.55	6.59E-07	33.76	1.25E-06	39.08
3.57E-07	28.73	6.54E-07	33.96	1.31E-06	39.33
3.67E-07	28.92	6.54E-07	34.18	1.36E-06	39.57
3.86E-07	29.19	6.58E-07	34.39	1.43E-06	39.83
3.86E-07	29.38	7.07E-07	34.61	1.43E-06	40.09
3.88E-07	29.66	7.36E-07	34.83	1.49E-06	40.32
3.98E-07	29.86	7.35E-07	35.06	1.67E-06	40.61
3.87E-07	30.04	7.59E-07	35.29	1.72E-06	40.84
4.55E-07	30.49	7.65E-07	35.53	1.82E-06	41.12
4.76E-07	30.67	7.70E-07	35.74	2.09E-06	41.39
4.84E-07	30.86	7.87E-07	36.10	2.39E-06	41.65
4.72E-07	31.06	8.10E-07	36.30	2.65E-06	41.92
4.75E-07	31.26	8.76E-07	36.65	2.70E-06	42.15
4.69E-07	31.45	9.00E-07	36.88	3.34E-06	42.47
4.66E-07	31.66	9.29E-07	37.13	4.12E-06	42.69
4.90E-07	31.86	9.90E-07	37.36	4.96E-06	43.02
5.21E-07	32.07	1.08E-06	37.61	5.46E-06	43.28
5.38E-07	32.37				

Appendix F - Ti 6-2-2-2-2 data in 177°C laboratory air at R = 0.1.

Fatigue crack growth rate (da/dN), cyclic stress-intensity (ΔK) and effective cyclic stress-intensity (ΔK_{eff}) data for two tests (one K-decreasing and one K-increasing) performed on T-L oriented Ti 6-2-2-2-2 in 177 °C laboratory air at R = 0.1 and 5 Hz is listed in Table F1. The tests were conducted in accordance with ASTM E 647 [7] with sinusoidal loading and the normalized K-gradient (C) for each test is listed in Table F1. This data is shown graphically in Figures 10, 11 and 13. Closure-free ΔK values, determined using the intersection of closure dominated and K_{max} affected results (as demonstrated in Fig. 8), for da/dN less than 1 x 10^{-7} m/cycle are also presented.

Table F1: Fatigue crack growth rate data for T-L oriented Ti 6-2-2-2-2 tested in 177 °C laboratory air at R = 0.1 and 5 Hz.

da/dN (m/cyl)	ΔK (MPa√m)	closure-free ΔK (MPa√m)	da/dN (m/cyl)	ΔK (MPa√m)	closure-free ΔK (MPa√m)
K-decreasing, C = -0.079 mm^{-1}			1.26E-09	3.60	2.50
2.24E-09	4.36	3.11	1.27E-09	3.57	2.51
2.25E-09	4.34	3.12	1.27E-09	3.55	2.51
2.20E-09	4.31	3.09	1.24E-09	3.53	2.49
2.22E-09	4.28	3.10	1.17E-09	3.51	2.44
2.23E-09	4.25	3.11	1.10E-09	3.49	2.39
2.19E-09	4.23	3.09	1.07E-09	3.47	2.37
2.10E-09	4.20	3.03	1.04E-09	3.45	2.35
1.92E-09	4.18	2.93	9.35E-10	3.43	2.27
1.84E-09	4.15	2.88	1.00E-09	3.40	2.32
1.87E-09	4.13	2.90	1.04E-09	3.39	2.35
2.05E-09	4.10	3.01	9.35E-10	3.36	2.27
2.25E-09	4.08	3.12	9.06E-10	3.35	2.25
2.20E-09	4.05	3.09	8.46E-10	3.33	2.21
2.02E-09	4.03	2.99	8.10E-10	3.31	2.19
1.97E-09	4.00	2.96	7.57E-10	3.29	2.15
1.91E-09	3.98	2.92	7.43E-10	3.27	2.14
1.79E-09	3.96	2.85	7.12E-10	3.25	2.12
1.78E-09	3.93	2.85	6.27E-10	3.23	2.07
1.75E-09	3.91	2.83	5.88E-10	3.21	2.04
1.70E-09	3.89	2.80	5.81E-10	3.19	2.04
1.65E-09	3.86	2.76	4.93E-10	3.17	1.99
1.66E-09	3.84	2.77	3.90E-10	3.15	1.96
1.66E-09	3.82	2.77	3.19E-10	3.13	1.95
1.62E-09	3.79	2.74	8.38E-11	3.11	1.93
1.61E-09	3.77	2.74			
1.56E-09	3.75	2.71			
1.49E-09	3.73	2.66	K-increasing, C=0.16 mm^{-1}		
1.43E-09	3.71	2.62	1.55E-09	3.55	2.70
1.38E-09	3.68	2.59	1.56E-09	3.61	2.71
1.35E-09	3.66	2.56	1.60E-09	3.65	2.73
1.31E-09	3.64	2.54	1.66E-09	3.69	2.77
1.25E-09	3.62	2.50	1.72E-09	3.74	2.81

Table F1. Continued

da/dN (m/cyl)	ΔK (MPa√m)	closure-free ΔK (MPa√m)	da/dN (m/cyl)	ΔK (MPa√m)	closure-free ΔK (MPa√m)
K-increasing, C=0.16 mm^{-1} (cont.)			7.28E-09	6.19	4.91
1.82E-09	3.78	2.87	7.59E-09	6.27	4.99
1.87E-09	3.83	2.90	7.88E-09	6.34	5.06
1.91E-09	3.88	2.93	8.20E-09	6.42	5.13
1.98E-09	3.92	2.97	8.69E-09	6.50	5.24
2.04E-09	3.97	3.00	9.07E-09	6.58	5.32
2.15E-09	4.02	3.07	9.36E-09	6.66	5.38
2.20E-09	4.07	3.09	9.62E-09	6.74	5.43
2.19E-09	4.12	3.09	9.99E-09	6.82	5.51
2.25E-09	4.17	3.12	1.05E-08	6.90	5.60
2.38E-09	4.22	3.19	1.11E-08	6.99	5.72
2.50E-09	4.27	3.26	1.16E-08	7.07	5.81
2.55E-09	4.32	3.28	1.21E-08	7.15	5.90
2.58E-09	4.37	3.30	1.27E-08	7.24	6.00
2.74E-09	4.42	3.38	1.30E-08	7.33	6.05
2.89E-09	4.48	3.45	1.37E-08	7.42	6.16
2.95E-09	4.53	3.48	1.44E-08	7.50	6.27
2.97E-09	4.59	3.49	1.49E-08	7.59	6.35
3.04E-09	4.64	3.52	1.55E-08	7.69	6.44
3.18E-09	4.70	3.58	1.59E-08	7.78	6.49
3.30E-09	4.75	3.63	1.68E-08	7.87	6.62
3.34E-09	4.81	3.65	1.77E-08	7.97	6.75
3.39E-09	4.87	3.67	1.81E-08	8.06	6.80
3.53E-09	4.93	3.73	1.87E-08	8.16	6.88
3.71E-09	4.99	3.81	1.99E-08	8.26	7.04
3.87E-09	5.05	3.87	2.07E-08	8.36	7.14
3.99E-09	5.11	3.92	2.15E-08	8.46	7.24
4.23E-09	5.17	4.01	2.25E-08	8.56	7.36
4.44E-09	5.23	4.08	2.33E-08	8.67	7.45
4.57E-09	5.30	4.13	2.43E-08	8.77	7.57
4.69E-09	5.36	4.17	2.61E-08	8.88	7.78
4.86E-09	5.42	4.23	2.71E-08	8.99	7.89
5.06E-09	5.49	4.29	2.79E-08	9.10	7.97
5.21E-09	5.56	4.34	2.92E-08	9.21	8.11
5.45E-09	5.62	4.41	3.01E-08	9.32	8.20
5.77E-09	5.69	4.51	3.09E-08	9.43	8.28
5.99E-09	5.76	4.57	3.22E-08	9.54	8.42
6.15E-09	5.83	4.62	3.41E-08	9.66	8.61
6.31E-09	5.90	4.66	3.58E-08	9.78	8.77
6.57E-09	5.97	4.73	3.67E-08	9.90	8.86
6.97E-09	6.05	4.84	3.67E-08	10.01	8.85
7.19E-09	6.12	4.89	3.81E-08	10.13	8.99

Table F1. Continued

da/dN (m/cyl)	ΔK (MPa√m)	closure-free ΔK (MPa√m)	da/dN (m/cyl)	ΔK (MPa√m)	closure-free ΔK (MPa√m)
K-increasing, C=0.16 mm^{-1} (cont.)			1.08E-07	14.88	
2.79E-08	9.10	7.97	1.13E-07	15.06	
2.92E-08	9.21	8.11	1.15E-07	15.25	
3.01E-08	9.32	8.20	1.17E-07	15.43	
3.09E-08	9.43	8.28	1.21E-07	15.62	
3.22E-08	9.54	8.42	1.26E-07	15.81	
3.41E-08	9.66	8.61	1.29E-07	15.99	
3.58E-08	9.78	8.77	1.32E-07	16.19	
3.67E-08	9.90	8.86	1.36E-07	16.38	
3.67E-08	10.01	8.85	1.39E-07	16.58	
3.81E-08	10.13	8.99	1.44E-07	16.78	
4.03E-08	10.25	9.19	1.48E-07	16.98	
4.15E-08	10.37	9.30	1.52E-07	17.18	
4.30E-08	10.50	9.43	1.54E-07	17.39	
4.44E-08	10.63	9.56	1.56E-07	17.61	
4.64E-08	10.76	9.73	1.61E-07	17.82	
4.86E-08	10.89	9.92	1.66E-07	18.04	
4.97E-08	11.02	10.01	1.70E-07	18.25	
5.26E-08	11.16	10.25	1.74E-07	18.48	
5.46E-08	11.29	10.41	1.80E-07	18.70	
5.51E-08	11.43	10.45	1.87E-07	18.92	
5.68E-08	11.56	10.59	1.93E-07	19.15	
5.83E-08	11.70	10.71	1.98E-07	19.38	
6.02E-08	11.85	10.85	2.03E-07	19.62	
6.20E-08	11.99	10.99	2.04E-07	19.85	
6.35E-08	12.13	11.11	2.06E-07	20.09	
6.52E-08	12.28	11.23	2.11E-07	20.34	
6.84E-08	12.43	11.47	2.17E-07	20.58	
6.99E-08	12.58	11.58	2.24E-07	20.83	
7.03E-08	12.73	11.61	2.34E-07	21.08	
7.33E-08	12.88	11.83	2.39E-07	21.34	
7.71E-08	13.04	12.10	2.41E-07	21.60	
8.01E-08	13.20	12.31	2.45E-07	21.86	
8.30E-08	13.36	12.51	2.49E-07	22.12	
8.72E-08	13.52	12.79	2.54E-07	22.38	
8.98E-08	13.68	12.96	2.61E-07	22.65	
9.15E-08	13.85	13.07	2.72E-07	22.92	
9.54E-08	14.01	13.33	2.80E-07	23.20	
9.84E-08	14.18	13.52	2.89E-07	23.48	
1.01E-07	14.36		2.96E-07	23.77	
1.04E-07	14.53		2.99E-07	24.06	
1.05E-07	14.70		3.03E-07	24.35	

Table F1. Continued

da/dN (m/cyl)	ΔK (MPa√m)	da/dN (m/cyl)	ΔK (MPa√m)	da/dN (m/cyl)	ΔK (MPa√m)
K-inc., C=0.16 mm^{-1} (cont.)		5.45E-07	35.83	1.88E-06	51.42
3.11E-07	24.64	5.53E-07	36.28	1.98E-06	52.03
3.18E-07	24.93	5.74E-07	36.71	2.20E-06	52.65
3.18E-07	25.24	5.91E-07	37.16	2.35E-06	53.28
3.21E-07	25.55	5.85E-07	37.61	2.44E-06	53.93
3.26E-07	25.86	5.94E-07	38.07	2.46E-06	54.53
3.35E-07	26.17	6.20E-07	38.53	2.65E-06	55.22
3.37E-07	26.48	6.52E-07	39.00	3.02E-06	55.87
3.38E-07	26.79	6.87E-07	39.46	3.15E-06	56.55
3.51E-07	27.12	6.86E-07	39.94	3.35E-06	57.27
3.64E-07	27.45	6.86E-07	40.42	3.80E-06	57.94
3.70E-07	27.79	7.15E-07	40.91	4.39E-06	58.65
3.77E-07	28.13	7.40E-07	41.40	4.68E-06	59.37
3.86E-07	28.48	7.84E-07	41.91	4.99E-06	60.12
3.92E-07	28.82	8.53E-07	42.41	5.08E-06	60.81
3.94E-07	29.16	9.32E-07	42.94	5.41E-06	61.59
3.98E-07	29.52	9.61E-07	43.45	7.04E-06	62.33
4.05E-07	29.87	9.58E-07	43.98	8.41E-06	63.16
4.08E-07	30.23	1.01E-06	44.51	8.57E-06	63.92
4.07E-07	30.59	1.02E-06	45.03	8.49E-06	64.77
4.09E-07	30.97	1.04E-06	45.58	9.34E-06	65.47
4.22E-07	31.33	1.13E-06	46.12	1.21E-05	66.28
4.38E-07	31.72	1.23E-06	46.68	1.36E-05	67.13
4.36E-07	32.09	1.28E-06	47.24	1.30E-05	67.99
4.46E-07	32.94	1.32E-06	47.81	1.64E-05	68.96
4.52E-07	33.34	1.42E-06	48.39	2.18E-05	69.79
4.50E-07	33.75	1.51E-06	48.96	2.81E-05	70.86
4.69E-07	34.17	1.59E-06	49.57	2.79E-05	71.60
4.90E-07	34.57	1.69E-06	50.18	3.78E-05	73.03
5.05E-07	35.00	1.81E-06	50.79	3.30E-05	73.78
5.33E-07	35.41				

REPORT DOCUMENTATION PAGE

Form Approved
OMB No. 0704-0188

1. AGENCY USE ONLY (Leave blank)	2. REPORT DATE	3. REPORT TYPE AND DATES COVERED
	March 2001	Technical Memorandum

4. TITLE AND SUBTITLE
Fatigue Crack Growth Characteristics of Thin Sheet Titanium Alloy Ti 6-2-2-2-2

5. FUNDING NUMBERS
706-61-11-02

6. AUTHOR(S)
Stephen W. Smith and Robert S. Piascik

7. PERFORMING ORGANIZATION NAME(S) AND ADDRESS(ES)
NASA Langley Research Center
Hampton, VA 23681-2199

8. PERFORMING ORGANIZATION REPORT NUMBER
L-18064

9. SPONSORING/MONITORING AGENCY NAME(S) AND ADDRESS(ES)
National Aeronautics and Space Administration
Washington, DC 20546-0001

10. SPONSORING/MONITORING AGENCY REPORT NUMBER
NASA/TM-2001-210830

11. SUPPLEMENTARY NOTES
Smith and Piascik: Langley Research Center, Hampton, VA
Work was performed while the first author was a National Research Council Resident Research Associate at Langley Research Center.

12a. DISTRIBUTION/AVAILABILITY STATEMENT
Unclassified-Unlimited
Subject Category 26 Distribution: Nonstandard
Availability: NASA CASI (301) 621-0390

12b. DISTRIBUTION CODE

13. ABSTRACT (Maximum 200 words)
Fatigue crack growth rates of Ti 6-2-2-2-2 as a function of stress ratio, temperature (24 or 177 °C), tensile orientation and environment (laboratory air or ultrahigh vacuum) are presented. Fatigue crack growth rates of Ti 6-2-2-2-2 are also compared with two more widely used titanium alloys (Timetal 21S and Ti 6Al-4V). The fatigue crack growth rate (da/dN) of Ti 6-2-2-2-2 in laboratory air is dependent upon stress ratio (R), particularly in the near-threshold and lower-Paris regimes. For low R (less than approximately 0.5), da/dN is influenced by crack closure behavior. At higher R (> 0.5), a maximum stress-intensity factor (Kmax) dependence is observed. Fatigue crack growth behavior is affected by test temperature between 24 and 177 °C. For moderate to high applied cyclic-stress-intensity factors (delta-K), the slope of the log da/dN versus log delta-K curve is lower in 177 °C laboratory air than 24 °C laboratory air. The difference in slope results in lower values of da/dN for exposure to 177 °C laboratory air compared to room temperature laboratory air. The onset of this temperature effect is dependent upon the applied R. This temperature effect has not been observed in ultrahigh vacuum. Specimen orientation has been shown to affect the slope of the log da/dN versus log delta-K curve in the Paris regime.

14. SUBJECT TERMS
Ti 6-2-2-2-2; Corrosion fatigue; Titanium alloys; Fatigue crack growth; Environmentally assisted cracking; Crack closure; Ti 6Al-4V; Timetal 21S

15. NUMBER OF PAGES
74

16. PRICE CODE
A04

17. SECURITY CLASSIFICATION OF REPORT	18. SECURITY CLASSIFICATION OF THIS PAGE	19. SECURITY CLASSIFICATION OF ABSTRACT	20. LIMITATION OF ABSTRACT
Unclassified	Unclassified	Unclassified	UL